AGU PUBLICATIONS

Geochemistry, Geophysics, Geosystems

RESEARCH ARTICLE
10.1002/2017GC006876

3-D basin-scale reconstruction of natural gas hydrate system of the Green Canyon, Gulf of Mexico

Ewa Burwicz[1], Thomas Reichel[2], Klaus Wallmann[1], Wolf Rottke[3], Matthias Haeckel[1], and Christian Hensen[1]

[1]GEOMAR Helmholtz Centre for Ocean Research Kiel, Kiel, Germany, [2]Statoil ASA, Oslo, Norway, [3]Schlumberger, Aachen, Germany

Key Points:
- Complex regional geology (i.e., salt tectonics and faulting) resolved with 3-D numerical modeling
- Methane gas recycling process identified at the base of the gas hydrate stability zone
- Total amount of gas hydrate predicted in the model domain (~450 km^2) equals ~340 Mt of carbon

Supporting Information:
- Supporting Information S1

Correspondence to:
E. Burwicz,
eburwicz@geomar.de

Citation:
Burwicz, E., T. Reichel, K. Wallmann, W. Rottke, M. Haeckel, and C. Hensen (2017), 3-D basin-scale reconstruction of natural gas hydrate system of the Green Canyon, Gulf of Mexico, *Geochem. Geophys. Geosyst.*, *18*, 1959–1985, doi:10.1002/2017GC006876.

Received 15 FEB 2017
Accepted 6 APR 2017
Accepted article online 12 APR 2017
Published online 18 MAY 2017

Abstract Our study presents a basin-scale 3-D modeling solution, quantifying and exploring gas hydrate accumulations in the marine environment around the Green Canyon (GC955) area, Gulf of Mexico. It is the first modeling study that considers the full complexity of gas hydrate formation in a natural geological system. Overall, it comprises a comprehensive basin reconstruction, accounting for depositional and transient thermal history of the basin, source rock maturation, petroleum components generation, expulsion and migration, salt tectonics, and associated multistage fault development. The resulting 3-D gas hydrate distribution in the Green Canyon area is consistent with independent borehole observations. An important mechanism identified in this study and leading to high gas hydrate saturation (>80 vol %) at the base of the gas hydrate stability zone (GHSZ) is the recycling of gas hydrate and free gas enhanced by high Neogene sedimentation rates in the region. Our model predicts the rapid development of secondary intrasalt minibasins situated on top of the allochthonous salt deposits which leads to significant sediment subsidence and an ensuing dislocation of the lower GHSZ boundary. Consequently, large amounts of gas hydrates located in the deepest parts of the basin dissociate and the released free methane gas migrates upward to recharge the GHSZ. In total, we have predicted the gas hydrate budget for the Green Canyon area that amounts to ~3256 Mt of gas hydrate, which is equivalent to ~340 Mt of carbon (~7×10^{11} m^3 of CH_4 at STP conditions), and consists mostly of biogenic hydrates.

Plain Language Summary Gas hydrates are ice-like crystalline deposits containing water and gas molecules. Gas hydrates are stable at low temperature and high pressure subseafloor environments. Due to their chemical composition, gas hydrates are proposed to be an important alternative source of energy. Our numerical modeling study performed on the Green Canyon site in the northern Gulf of Mexico shows that about 340 Mt of carbon can be potentially stored at this location which confirms its high economic potential.

1. Introduction

Reactive gas hydrate formation and accumulation in marine sediments was initially simulated using simple 1-D models [e.g., *Baba and Katoh*, 2004; *Davie and Buffett*, 2001, 2003; *Garg et al.*, 2008; *Katoh et al.*, 2000; *Rempel and Buffett*, 1997]. Subsequently, these models were augmented to include the Anaerobic Oxidation of Methane (AOM) [e.g., *Burwicz et al.*, 2011; *Chatterjee et al.*, 2011; *Egeberg and Dickens*, 1999; *Torres et al.*, 2002; *Wallmann et al.*, 2006], the permeability evolution due to gas hydrates formation [*Nimblett and Ruppel*, 2003; *Seol and Kneafsey*, 2011], and the influence of a free-gas layer underlying gas hydrate deposits [*Bhatnagar et al.*, 2007]. Two-dimensional models were developed to simulate gas hydrate formation at passive continental margins and accretionary wedges considering biogenic and thermogenic sources of methane, the effects of AOM, and migration of dissolved and gaseous methane [*Archer and Buffett*, 2012; *Archer et al.*, 2012; *Milkov and Sassen*, 2003]. More recently, a commercial PetroMod® basin modeling software was introduced as a gas hydrate modeling tool [*Pinero et al.*, 2016] by simulating gas hydrate formation from both biogenic and thermogenic methane sources in a highly idealized three-dimensional layer-cake model. This new software tool was successfully used to predict the temporal evolution of the gas hydrate stability zone (GHSZ), the accumulation of gas hydrates, multiphase migration on a large basin scale, and the influence of faults on migration pathways. Moreover, it was used to investigate gas generation and methane hydrate

formation in two dimensions at the subduction margin of New Zealand [*Kroeger et al*., 2015]. That study predicted prominent gas hydrate deposits within sandy Hikurangi channel layers formed by the ascent of thermogenic gas from great depth. As pointed out by the authors, the lack of a third dimension in the model seemed to limit this numerical approach and make the quantitative methane flux analysis somewhat difficult. Nevertheless, a good fit of gas hydrate concentrations between model predictions and estimates derived from seismic data was obtained with a slight vertical misfit.

This contribution presents the first attempt to simulate gas hydrate formation employing a 3-D basin modeling approach considering the full complexity of natural geological system using the Gulf of Mexico as a case study. The model is based on a thermal and depositional basin reconstruction including the development of multiple faults and considers salt tectonics introduced as a propagating salt front. High lateral as well as vertical resolution of the model (results obtained with up to ~1 m precision) allows for direct comparison of modeling output with reported well data. The detailed temporal evolution of the GHSZ and gas hydrate deposition was reconstructed considering methane gas accumulations and losses over the entire basin history (Jurassic-present).

2. Study Area

2.1. Geological Setting and Basin Evolution

The Green Canyon area is located in the northern part of the Gulf of Mexico, at the edge of the NE-SW directed Mississippi frontal fold belt (see Figure 1), at water depths of about 2000 m. The name of the province refers to the important paleo-channel-levee complex of sandy sediments deposited toward the deep abyssal plain of the central Gulf. Prominent buried paleo-channel systems in the region can be clearly identified on seismic images [*Boswell et al*., 2012a, 2012b; *Diegel et al*., 1995; *Hutchinson et al*., 2011; *Salvador*, 1991;

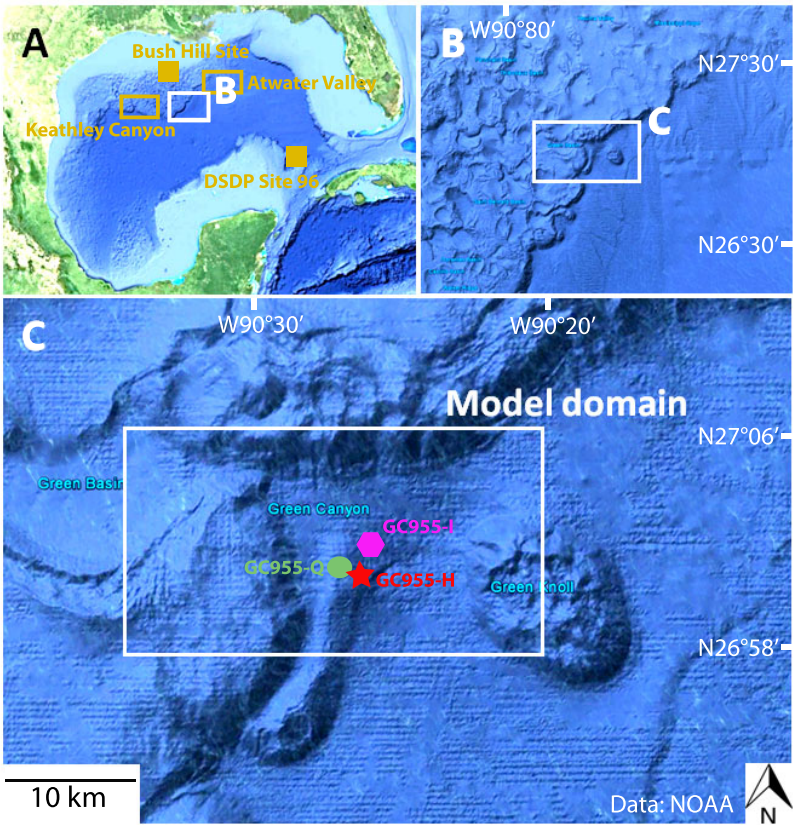

Figure 1. Seafloor maps of the (A) Gulf of Mexico basin with marked locations of the Keathley Canyon, Atwater Valley, Bush Hill Site, and DSDP Site 96, (B) the northern part of the basin, and (C) the Green Canyon area. The white rectangle on the lower picture (C) shows the location and boundaries of the numerical model domain (with X and Y dimensions of about 32 × 14 km), together with the locations of JIP Leg II drill wells GC955-I (violet), GC955-Q (green), and GC955-H (red).

Shedd et al., 2012] due to large portions of siliciclastic material delivered from the NW direction toward deeper parts of the basin over the Pleistocene. The modeling domain chosen for this study is situated at the edge of the allochthonous salt front which represents some of the last stages of salt tectonic remobilization in the region and covers the area of about 32 × 14 km (see Figure 1). The evaporite deposits have a strong effect on the subsurface migration of petroleum components [*McBride et al*., 1998; *Weimer et al*., 1998].

The evolution of the northern part of the Gulf of Mexico basin was initiated by a Late Triassic-Early Jurassic event of North American and African-South American plate separation as a result of a crustal stretching and thinning processes. Subsidence during the Mesozoic era was especially large in the central part of the basin; however, the northern part of the Gulf received the largest sedimentary load over the Cenozoic. The total amount of sediments within the northern part of the basin is estimated at 10–15 km [*Salvador*, 1991] or 12–15 km [*Van Avendonk et al*., 2015] and contains of Lower Jurassic to Holocene layers deposited over the life-span of the basin. For the purpose of this study, the basement was set to a depth of 14,500 m below the sea level which stays within the consensus range of reported values.

Geophysical data indicate that gas hydrate and free gas are present in the region and are either largely confined to a narrow horizon that most likely represents the base of the gas hydrate stability zone (around 400–500 mbsf) or, in general, present in the deepest ∼200 m of the GHSZ. Three wells drilled within the area during the Joint Industry Project (JIP) Leg II campaign (see locations of well GC955-I, GC955-Q, and GC955-H in Figure 1) provide important information on the character of the Pleistocene sediments and their potential to host gas hydrate and free-gas accumulations [*Guerin et al*., 2009; *Lee and Collett*, 2012; *Zhang et al*., 2011]. A detailed analysis of the drilling site location before the JIP Leg II campaign [*Hutchinson et al*., 2009] revealed abundant faulting structures in the surrounding of salt deposit heights and their direct vicinity confirming the existence of high-permeability pathways for gas migration necessary to transport sufficient amounts of methane into the GHSZ. Direct observations obtained during the drilling process confirmed the presence of both fracture and pore-filling gas hydrate accumulations for at least two of the three wells (see detailed description in section 3.2).

2.2. Stratigraphy

The oldest syn-rift Upper Triassic-Lower Jurassic material deposited in the northern part of the Gulf of Mexico basin contains mostly siliciclastics of nonmarine origin. During the Callovian age (upper Middle Jurassic) thick accumulations of evaporites started to form throughout the basin [*Bird et al*., 2005; *McBride et al*., 1998]. These extensive Louann Salt deposits are uniquely large and dominate the geometry of the basin which is also controlled by preexisting large-scale structures such as basement fault blocks related to the earliest stage of basin rifting [*Stephens*, 2001, 2009]. Following the change from a terrestrial to shallow marine conditions, carbonate deposits started to form from the Late Jurassic to Early Cretaceous period. The deeper part of the basin experienced shale and pelagic carbonate ooze depositions. A clearly defined Middle Cretaceous unconformity level (sequence boundary) marks the time when siliciclastic sediments started to dominate the lithology. Shales and silts were the most abundant formations at the end of the Cretaceous period. They were delivered to the northern Gulf in response to the Sevier and the simultaneously occurring Laramide orogeny, which were responsible for the formation of several mountain ranges in North America and Mexico.

Thick sandy Pleistocene accumulations are the result of channel-levee systems and deep water fans, which potentially serve as high-porosity and permeability petroleum and gas hydrate reservoirs. Figure 2 presents a simplified lithostratigraphic column of the northern Gulf of Mexico indicating stratigraphic locations of three distinct source rock levels used in this study (Upper Jurassic: Oxfordian and Tithonian; Upper Cretaceous: MCU [*Hood et al*., 2002]), the location of primary hydrocarbon reservoir rocks, and horizons of known age identified in the course of seismic data interpretation.

2.3. Salt Tectonics and Related Faulting Systems

Due to their distinct thermal and physical properties (high thermal conductivity and low permeability), salt deposits play an important role in hydrocarbon maturation and migration. The perfect sealing provided by evaporites redirects the flow of hydrocarbons and strongly influences their migration pathways. For the purpose of this study, it was thus essential to capture the right timing of allochthonous salt movement and other events inducing salt remobilization and thickness variations within the spatial boundaries of the

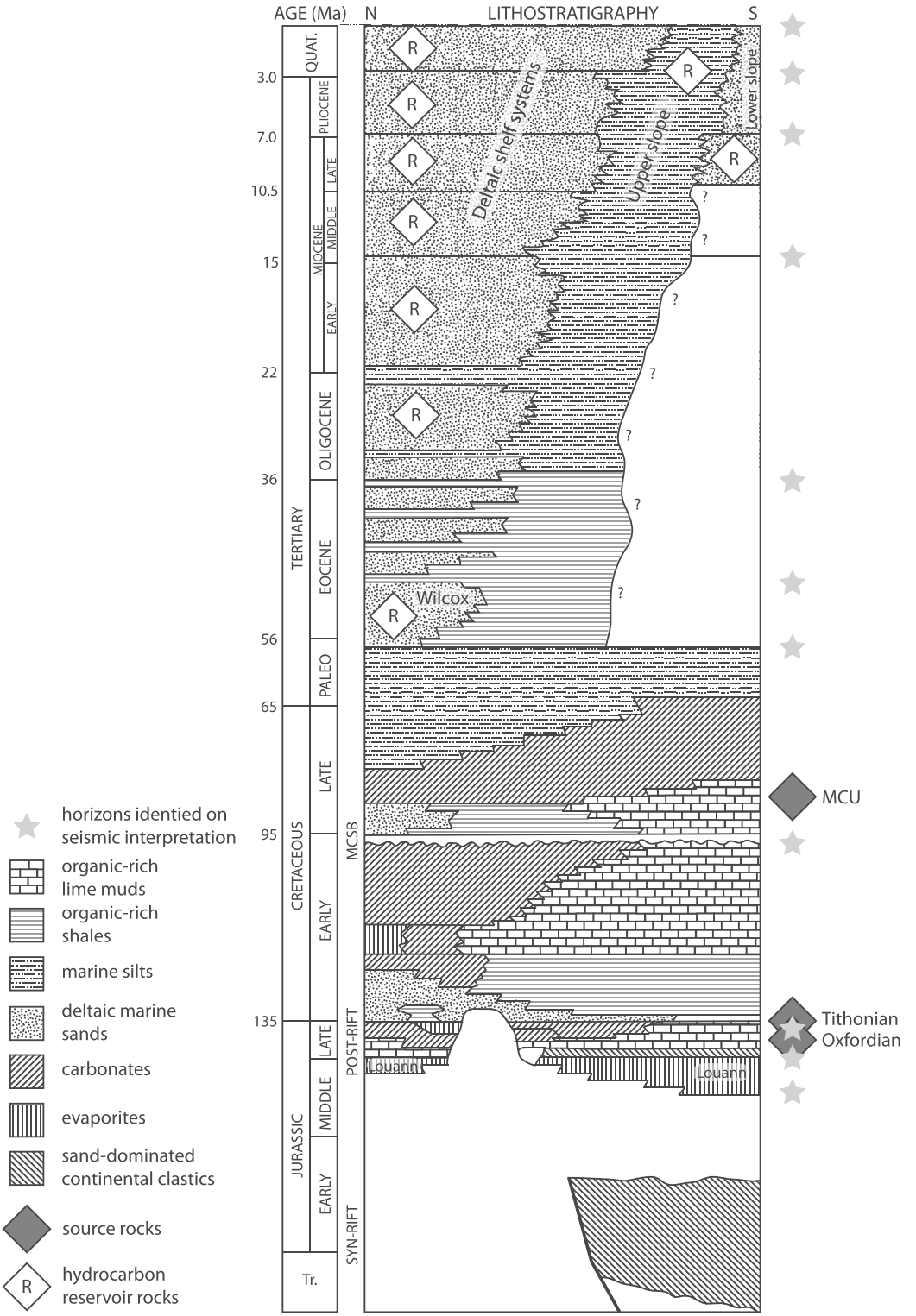

Figure 2. Lithostratigraphy of the northern Gulf of Mexico (modified after *Piggott and Pulham* [1993]) presenting the most important lithostratigraphic units, locations of three source rocks used in the study (black diamond symbols), and hydrocarbon reservoir rocks (white diamond symbols). Moreover, locations of stratigraphic horizons clearly identified during seismic interpretation are marked by gray stars.

considered 3-D domain. The schematic illustration presented in Figure 3 shows a simplified present-day NW-SE transect across the northern Gulf of Mexico (modified after *Prather* [2003]), based on published data from *Diegel et al*. [1995] with abundant salt-withdrawal-intraslope minibasins, which currently dominate the

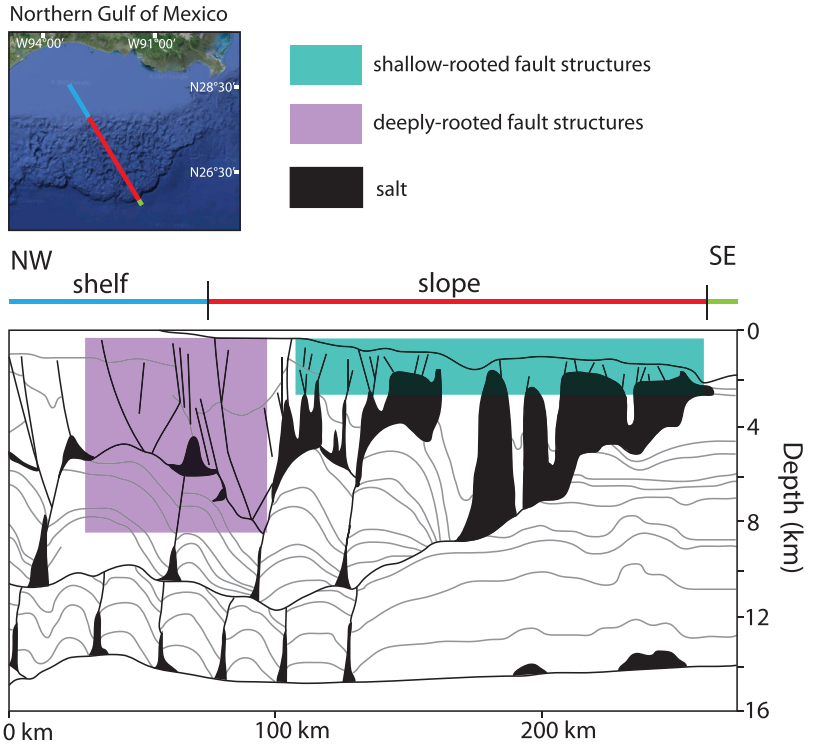

Figure 3. Simplified interpretation of posttectonic structures and salt deposits in the northern part of the Gulf of Mexico (modified after *Prather* [2003]), based on published data from *Diegel et al.* [1995]. Deeply rooted fault structures (violet shading) developed due to large-scale salt remobilization events while shallow-rooted fault structures (green shading) formed directly above rising salt domes. Shelf, continental slope, and abyssal regions are indicated as blue, red, and green solid lines, respectively, in the map of the area (upper part) and above the cross section (lower part).

subsurface geometry of the sedimentary system. A complex network of highly permeable pathways (i.e., faults) associated with salt structures is commonly observed in the region [*Boswell et al.*, 2012a; *Diegel et al.*, 1995; *Prather*, 2003]. It is characterized by (a) shallow-rooted faulting structures developing directly above the rising salt diapirs and (b) deeply rooted faulting structures associated with progressive and large-scale salt mobilization in SE direction. These two distinct types of structural disconformities are schematically presented in Figure 3 as shallow-rooted fault structures (green shading) and deeply rooted fault structures (violet shading).

Impermeable salt deposits can form a physical barrier for vertical fluid and gas migration and thus constitute an important part of the regional petroleum system. It is commonly observed that migration pathways of pore fluids and free gas tend to deflect laterally directly underneath salt accumulations and continue migrating along the base of the salt layer until reaching a local topographic high or structural unconformity, e.g., tectonic fault. The amounts of gas accumulated under impermeable salt layers are usually not sufficient to fracture the overlying evaporites due to rather low local overpressures. Commonly, faults related to salt remobilization events in the area are generally steep and represent major pathways for fluid and gas migration, typically limiting lateral distribution of fluids. In case of gas migration through the faulting structures, buoyancy seems to be the driving factor enhanced by local gas overpressure zones.

2.4. Presence of Gas Hydrates

The presence of gas hydrate deposits (both pore space-filling and fracture-filling) has been confirmed in the Green Canyon area [*Boswell et al.*, 2012a, 2012b; *Hutchinson et al.*, 2009; *Lee and Collett*, 2012; *McConnell et al.*, 2010; *Zhang et al.*, 2011] by seismic data analysis (abundant high-amplitude geophysical responses, continuous and discontinuous BSRs after *Shedd et al.* [2012]), geochemical data and wellbore LWD measurements (JIP Leg II resulting in GC955-H, GC-955-I, and GC955-Q drill sites with locations shown in Figure 1). In addition, widespread gas hydrate occurrence in the Green Canyon region has been postulated based on

the presence of porous sandy layers close to the base of the GHSZ and highly permeable pathways for gas and fluid migration. The JIP campaign was conducted in order to validate the hypothesis of prominent gas hydrate accumulations close to the base of the GHSZ which might be acting as a physical barrier for further upward migration of a free gas. Two of the three wells (GC955-H and GC-955-I) penetrated the entire GHSZ and underlying sediment sequences down to 550 and 650 mbsf, respectively, whereas well GC955-Q terminated at the inferred base of the GHSZ located at a depth of about 460 mbsf. As it was reported after conducting the JIP drilling campaign [*Boswell et al*., 2012b; *Guerin et al*., 2009; *Lee and Collett*, 2012; *Zhang et al*., 2012], sediments drilled at site GC955-H revealed thick gas hydrate-filled fractures within fine-grained sediments at depths of about 152–305 mbsf with average gas hydrate saturations of about 20% with respect to the pore volume. Furthermore, three distinct gas hydrate-bearing zones were identified within sandy sediments between 400 and 500 mbsf with an average gas hydrate saturation of about 60–80 vol %. Well GC955-Q exposed prominent gas hydrate accumulations at depths of 430 down to 457 mbsf, most likely turning into free-gas deposits at greater depths. However, the drilling procedure was stopped at this depth to avoid the high risk of gas migration through the well. In general, four main logging units were commonly defined based on LWD data [*Guerin et al*., 2009]: Unit 1 characterized by a smooth transition in lithology from marine interbedded clays (near the seafloor zone) to sand (base of the unit at the depth of about 280 mbsf for wells GC955-I and GC955-Q and 225 mbsf for well GC955-H), Unit 2 built up by sandy paleo-levee systems extending up to depths of about 360–405 mbsf, Unit 3 with a similar lithology to Unit 2 but showing apparent evidence for high gas hydrate saturations based on electrical resistivity values particularly at drill holes GC955-H and GC955-Q up to the depth of about 480 mbsf, and Unit 4 reached only by GC955-H and GC955-I, marking the change in lithology to clay-rich sediments with indications for the presence of either free gas or gas hydrate.

Geochemical and carbon isotope studies conducted at the upper and middle slope of the northern Gulf of Mexico (the Bush Hill site) [*Milkov and Sassen*, 2000] suggest a mixed-biogenic and thermogenic origin of methane within the GHSZ. However, *Lorenson et al*. [2008] based on gas samples recovered from the Atwater Valley and the Keathley Canyon (northern Gulf of Mexico) postulates mostly biogenic methane origin with very little thermogenic gas input. As a source of analyzed methane, the authors suggest early diagenesis of organic matter and possibly petroleum biodegradation. Moreover, bacterial methane sources are probably not limited to shallow Pleistocene sedimentary layers but may extend to larger depths of the Green Canyon block being related to high-temperature microbial activity in relatively old sediments [*Sassen et al*., 2003]. Moreover, the complex burial history of the basin probably allowed for multiple episodes of gas recharge that complicate the reconstruction of gas production at basin scale. In the present study, we quantified the amount of gas hydrates formed within the Green Canyon domain via both microbial in situ decomposition of organic matter and thermogenic methane generation at great depth. We also analyzed the proportions between both sources in a series of test runs over a range of Pleistocene TOC contents and primary Tithonian source rock productivities (see supporting information and section 5 for details).

2.5. Petroleum Geology of the Region

The northern Gulf of Mexico has been considered as a complete petroleum system including source rocks generating hydrocarbons, efficient hydrocarbon migration pathways as well as suitable reservoir rocks [*Nunn and Sassen*, 1986]. Due to the lack of deep drilling data, source rocks were studied by geochemical, biomarker and whole-rock analysis performed onshore Louisiana for the same stratigraphic layers drilled offshore by the Deep Sea Drilling Project (DSDP).

There are three source rocks of different productivities indicated to be present within the modeling domain of the Green Canyon, situated on three different stratigraphic levels (Figure 2): (i) Late Jurassic-Oxfordian, (ii) Late Jurassic-Tithonian, and (iii) Middle Cretaceous-MCU named after the mid-Cenomanian unconformity stratigraphic level [*Cole et al*., 2001; *Nunn and Sassen*, 1986; *Piggott and Pulham*, 1993; *Sassen*, 1990]. Although the Oxfordian and MCU source rocks are thought to contribute to the petroleum formation in the northern Gulf of Mexico, most of the hydrocarbons seem to originate from the Tithonian source rock.

The source rocks contain mainly type II kerogen with rare exceptions of type II-S (enriched in sulfur) and gas-generating type III kerogen [*Sassen and Macdonald*, 1994]. Initial TOC and HI values for the northern Gulf of Mexico source rocks are difficult to deduce from available data. The complex burial history and presence of allochthonous salt layers influence the thermal maturation and thus there are productivity peaks for

Table 1. Source Rock Properties Used in the Modeling Study[a]

Source Rock	Tithonian (Upper Jurassic)	Oxfordian (Upper Jurassic)	MCU (Middle Cretaceous)
Importance	Primary	Secondary	Secondary
Lithology	Marls/carbonates	Marls/carbonates	Shales to marls
TOC content	4–6 wt %	About 3 wt %	2–3 wt %
TOC content used in the study	6 wt %	3 wt %	3 wt %
HI	550–700 mg HC/g TOC	450–550 mg HC/g TOC	200–500 mg HC/g TOC
HI used in the study	640 mg HC/g TOC	550 mg HC/g TOC	500 mg HC/g TOC
Thickness	80–200 m	About 50 m	30–50 m
Thickness used in the study	200 m	50 m	50 m
Secondary cracking	Yes	Yes	Yes
HC generation kinetics based on	Type II kerogen [*Burnham*, 1989]	Type II kerogen [*Burnham*, 1989]	Type II kerogen [*Burnham*, 1989]

each source rock in space and time. These result in overlapping productivity stages of particular source rock levels which, together with widespread salt tectonics modulates and controls the gas migration potential into gas hydrate reservoir sands of Pleistocene age. However, migration pathways from all hydrocarbon generation layers seem to be similar and shared among the three source rocks present [*Cole et al*., 2000]. In this study, we assume the following source rock parameters (Table 1).

Biogenic methane generation, previously suggested as potentially prominent CH_4 source in the shallowest Pleistocene sediments of the Green Canyon region [*Kennicutt et al*., 1986; *Lorenson et al*., 2008; *Rice*, 1980], has been modeled using a simple kinetic rate law relating the reactivity of organic material to its depositional age [*Middelburg*, 1989]. It was incorporated into the PetroMod™ software biodegradation module assuming 1 wt % TOC content and HI = 100 mg HC/g TOC (see section 3.9). The additional sensitivity analyzes were performed assuming (a) Tithonian layer thickness reduced to 80 m (supporting information Figure S3), (b) Tithonian layer thickness reduced to 150 m (supporting information Figure S4), (c) Tithonian layer thickness reduced to 140 m, Tithonian TOC content set to 5 wt % and HI set to 625 mg HC/g TOC (supporting information Figure S5), and (d) reduced initial TOC input in the Pleistocene layers equal 0.7 wt % (supporting information Figure S6). However, it was expected that the chosen Tithonian source rock properties have no significant effect on the present-day gas hydrate accumulations due to their predominantly biogenic origin. For the purpose of the reference run, we employed maximum estimates for the Tithonian POC content to support our conclusion that hydrates are formed from biogenic rather than thermogenic methane.

3. Modeling Approach

This 3-D modeling study was conducted employing the PetroMod™ software package v. 2014.1 by Schlumberger. The basin analysis approach in the PetroMod™ software package is based on the back-stripping method which uses the present-day geometry of the basin to reconstruct initial layer thicknesses and densities together with the ages of deposition. This method assumes conservation of mass and allows for tracking back the evolution of particular geological facies and lithologies in time within the region of interest. Employing well data and other accessible data sources, it is possible to define physical properties for each modeled sediment layer (e.g., initial seafloor porosity, compaction length scale as used in Athy's law formulation [*Athy*, 1930], density, permeability, and sealing properties), as well as their thermal properties (e.g., thermal conductivity, heat capacity, and radiogenic heat), and specific gas hydrate-related features (e.g., methane diffusion in pore fluids, gas hydrate formation and dissolution, presence of in situ organic matter and its decomposition into methane). Sedimentation rates were derived from the age and original thickness of the deposited layers. No significant events of erosion were reported for the geological history of the Green Canyon region and thus they were not considered in our study.

Boundary conditions including heat flow, temperature, and paleo-bathymetry were assigned to the model (section 3.5) together with faults serving as high-permeability pathways for gas ascent (section 3.4), and allochthonous salt layers (section 3.3). Source rocks present in the model were characterized by assigned

TOC and HI values (Table 1) as well as hydrocarbon generation kinetics which define the temporal evolution of oil and gas production (see section 3.9 for details).

3.1. Surface Maps and Age Assignment

The 3-D model contains 196 horizons covering strata from the Lower Jurassic basement to the present seabed. Twenty-eight of these horizons were interpreted directly from the depth-converted 2-D and 3-D conventional exploration seismic data (i.e., high-quality multiclient data sets). Unfortunately, these data sets are not publically available. The remaining 168 horizons result from layer splitting performed on the uppermost thick Pleistocene and Upper Miocene (subsalt) package to increase the vertical resolution of the model in order to achieve a better control on potential gas hydrate formation in the reservoir layers as well as subsalt gas migration, respectively. Splitting of the horizons was performed employing a uniform thickness distribution. Special attention was paid to avoid depth overlapping (crossing) of the horizons and, where necessary, manual correction on the seismic interpretation was applied. Each of the 196 sedimentary layers was defined as a distinct sediment package stretching between 3-D depth horizons. The deposition age of each sedimentary package was derived from the stratigraphic sequence of the Green Canyon region [*Boswell et al*., 2012a; *Shedd et al*., 2012; *Witrock et al*., 2003]. Publicly released calcareous nannofossil data from the Gulf of Mexico exploration wells nearby have been used for the stratigraphic control in relation to the released biostratigraphic framework published by *Witrock et al*. [2003]. Some Jurassic ages could only be estimated due to the lack of precise data. Age units clearly identified in the model comprise Lower, Middle, and Upper Jurassic sediments, Middle Cretaceous unconformity, Upper Cretaceous sediments, Wilcox unit strata, Intra Eocene sediments, several lithologically distinct layers of Oligocene and Miocene age, thin Pliocene and thick Pleistocene sediment packages. The deeper horizon interpretation (older than Pleistocene) is based on regional in-house seismic interpretation, based on well ties to key wells which are available to Statoil.

Finally, a uniform X and Y-direction resolution was applied to all interpreted depth maps and, consequently, to sedimentary layers defined between the upper and lower horizon of each section. As a result, we obtained a 3-D model with a 256 $\times$ 256 grid points in the XY direction, which refers to a resolution of 128 m $\times$ 53 m in X and Y direction, respectively (Figure 4). The vertical resolution depends on the layer geometry and varies between 1 and 31 m in Z direction (depending on the grid cell location) for the uppermost sedimentary layers located within the GHSZ allowing for a precise comparison between modeling results and drill well log data.

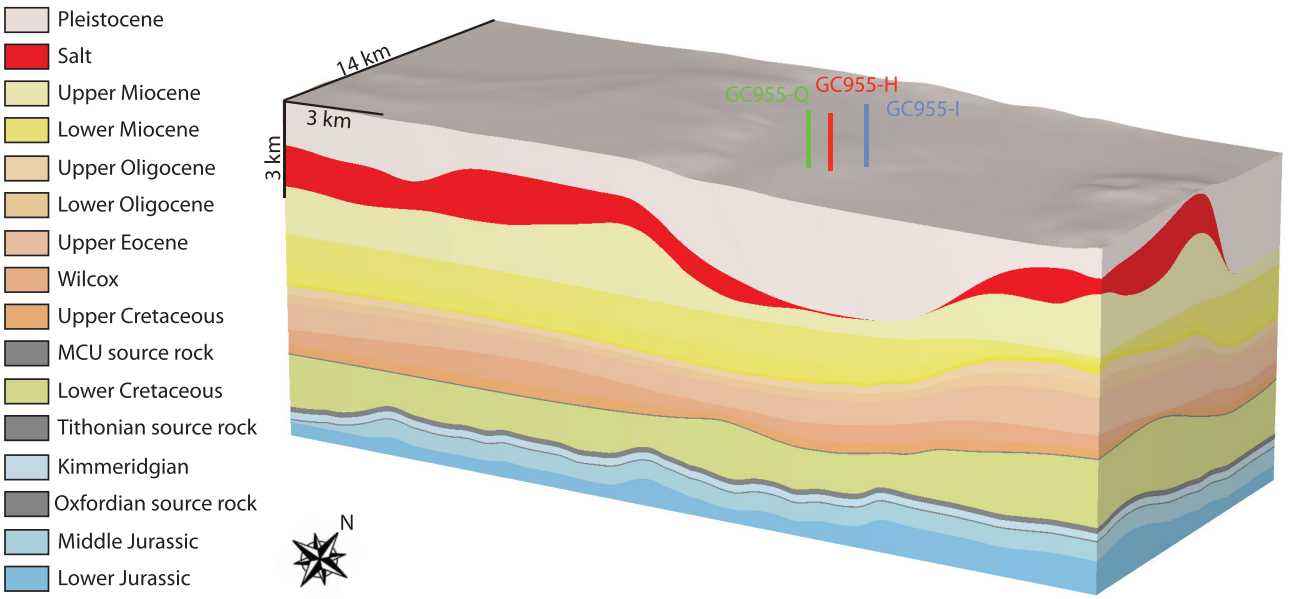

Figure 4. Stratigraphy and geometry of the 3-D model domain. JIP Leg II drill wells GC955-I (blue), GC955-Q (green), and GC955-H (red) marked with blue, green, and red solid lines, respectively. Oldest stratigraphic layers recognized in the region represent Lower Jurassic sediments-basement of the modeling domain is assumed to be located at a depth of 14,500 m below the sea level.

Table 2. Summary of Main Sedimentary Facies and Their Properties Used in the Study (Pli-Pliocene, Pleis-Pleistocene, Mio-Miocene, Oli-Oligocene, Pal-Paleocene, Eo-Eocene, Cretac-Cretaceous, and Jur-Jurassic)[a]

Facies Type	Ages	Initial Porosity	Compaction Length Scale	Heat Capacity at 20°C	Thermal Conductivity at 20°C	Radiogenic Heat Production U/Th/K
Sandstone	Pli, Pleis, Mio, Oli, Pal, Eo	59%	0.5 km^{-1}	0.21 kcal/kg/K	3.46 W/m/K	1.44 ppm/3.8 ppm/1.24%
Siltstone	Pleis, Mio, Oli	65%	0.65 km^{-1}	0.22 kcal/kg/K	2.05 W/m/K	2 ppm/5 ppm/1%
Sandstone-siltstone mixed lithology	Pli, Pleis	63–59%	0.55–0.6 km^{-1}	0.21 kcal/kg/K	3.29–2.66 W/m/K	1.5 ppm/3.92 ppm/ 1.22%–1.72 ppm/4.4 ppm/1.12%
Marl	Eo, Pal, Cretac, Jur	50%	50 km^{-1}	0.20 kcal/kg/K	2.00 W/m/K	2.5 ppm/5 ppm/2%
Shale	Mio	70%	0.83 km^{-1}	0.21 kcal/kg/K	1.64 W/m/K	3.7 ppm/12 ppm/2.7%
Salt	Mobilized in Neogene	Not compactable		0.21 kcal/kg/K	6.50 W/m/K	0.02 ppm/0.01 ppm/0.1%

[a]Sandstone-siltstone mixed lithology was prescribed by a mixing law in proportions ranging from 90 to 10% to 40 to 60% of sandstone and siltstone, respectively.

3.2. Lithology, Facies Definitions, and Sediment Properties

The lithology of each sedimentary layer was derived from northern Gulf of Mexico stratigraphy publications [*Piggott and Pulham*, 1993], Green Canyon reports [*Guerin et al*., 2009; *Hutchinson et al*., 2009; *Lee and Collett*, 2012], and data from drilling campaigns performed in the Green Canyon region and its vicinity (i.e., industry drill wells GC955 #001 and GC955 #002 after *McConnell* [2000] and *Hutchinson et al*. [2009]). The main stratigraphic levels derived from seismic observations were employed to define individual horizons and their deposition ages. In case of unknown lithologies or too vague descriptions in literature (e.g., Mesozoic synrift and postrift siliciclastics, postmiddle Cretaceous unconformity shales and silts, etc.), standard physical properties of the indicated lithology were taken from the default software library. Table 2 compiles the main sedimentary facies and their mechanical as well as thermal properties used in the modeling study. Permeability of each layer was calculated from Kozeny Carman model that accounts for depth-dependent porosity changes and the specific surface area of grains of a given lithology kind. In case of the mixed lithologies (sandstone-siltstone, see Table 2), facies permeabilities (horizontal and vertical) were mixed geometrically.

Whenever possible, compaction properties of the youngest Pleistocene sediments such as initial seafloor porosity and compaction length scale were derived by direct correlation with well data and published porosity profiles of the three Green Canyon wells drilled during the JIP Leg II campaign [*Guerin et al*., 2009]. Figure 5 presents porosity data points for three Green Canyon drill sites (GC955-I, GC955-Q, and GC955-H) and the modeling result (solid curve) extracted from the 3-D modeling domain at the well location. Unfortunately, a notable washout due to borehole enlargement occurred in gas-prone sections of all wells which makes density and neutron porosity data unreliable (specifically in the sand-rich sediments interval between 420 and 525 mbsf for well GC955-H, below 390 mbsf for well GC955-I, and ~98 mbsf and ~411 mbsf for well GC955-Q) [*Guerin et al*., 2009]. This correlation of preliminary modeling results with measured data obtained during the JIP Leg II drilling campaign (i.e., porosity) was further used to recalibrate the numerical model before performing the high-resolution test runs. Gas hydrate saturations derived from the LWD data were not used for the model calibration at any stage. As the gas hydrate saturations based on the LWD technique were the only available data, they were further used to draw the conclusions about the final model results.

3.3. Salt Tectonics and Related Phenomena

To account for the kinematics of the salt layer and its evolution in space and time, we constructed a set of paleo-thickness maps defining the change of salt volume, location, and thickness. Since the lithology of sedimentary layers in the model does not vary horizontally and the model does not contain major shale formation directly underneath the salt which might result in additional "doming" of this formation, we assumed a homogeneous (linear) mechanism of salt expansion within the entire study area. Temporal and spatial changes in salt layer thickness incorporate processes of layer stretching and thinning to achieve a present-day geometry at the end of the simulation.

The salt layer is assumed to have perfect sealing properties inhibiting flow of fluid or gas (see Table 2). Physical properties of the salt layer that might influence the spatial extent of the gas hydrate stability zone (e.g., extremely high thermal conductivity, low permeability, and incompressibility) were considered and defined employing the values from the default software library (e.g., temperature-dependent thermal conductivity).

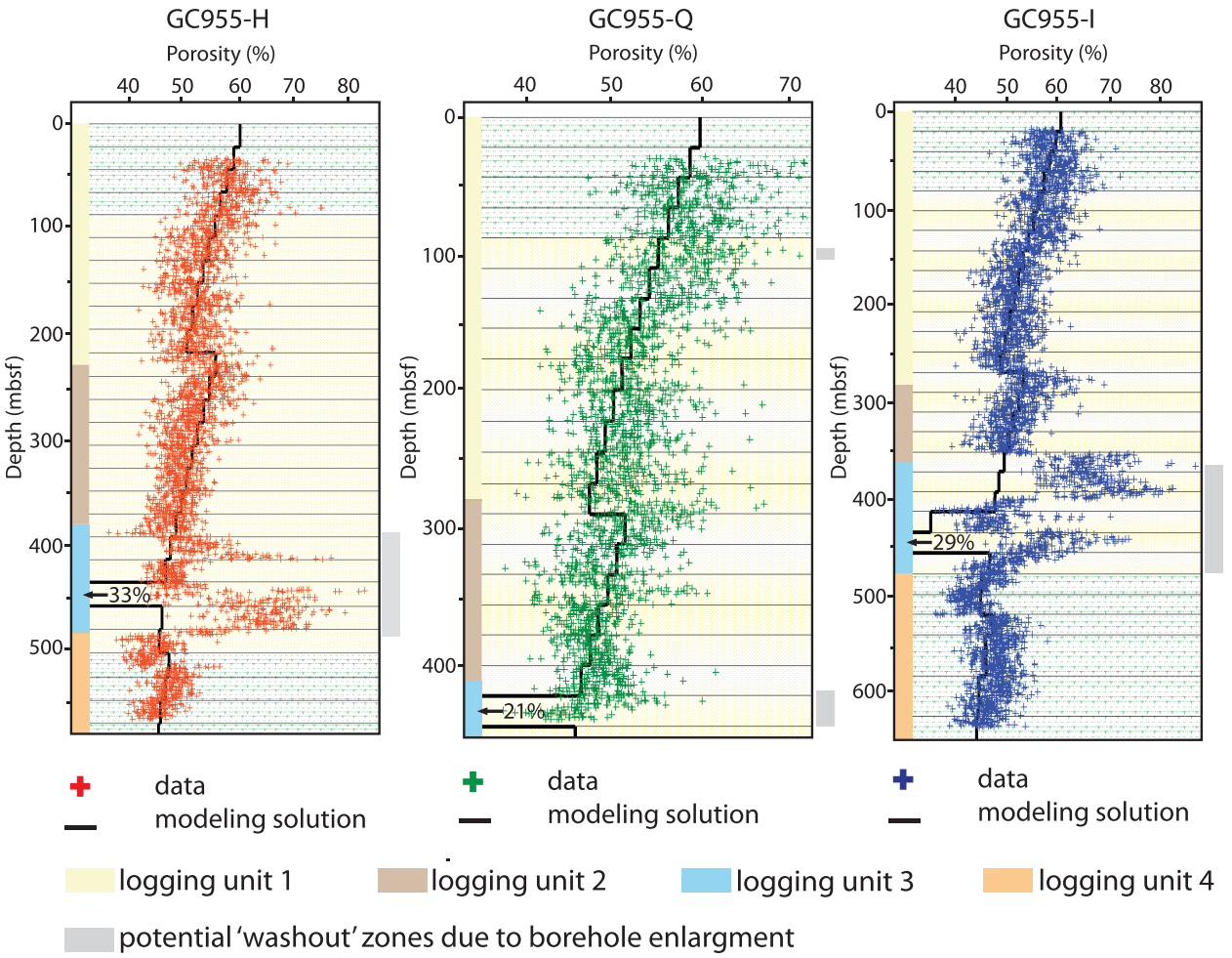

Figure 5. Porosity data from drill wells GC955-H (in red), GC955-Q (in green), and GC-955-I (in blue) plotted together with sediment porosity calculations performed for each well (solid black lines) in the uppermost Pleistocene layers. Yellow, brown, blue, and orange shadings mark the position of logging units 1, 2, 3, and 4, respectively defined after *Guerin et al.* [2009]. Gray shading indicate the location of potential "washout" zones based on drilling reports where measured porosity might not fit the actual porosity present at that depths. Porosity decrease at depths around 430–450 mbsf visible in the numerical solution (black solid line) is caused by a predicted presence of high-saturation gas hydrate deposits close to the base of the GHSZ. Background color reflects lithological differences, yellow horizons represent sand-dominated layers while green horizons represent clay-dominated sediments.

3.4. Faults and High-Permeability Conduits

Structural discontinuities present in the region were identified from seismic imaging (see Figure 3) and grouped into two main categories presented in Figure 6: (i) deeply rooted faulting structures associated with multiple salt remobilization events and (ii) shallow-rooted faulting structures representing sediment response to underlying salt dome rising and layer deformation, usually recognized as normal faults associated with high probability of active fluid flow [*McConnell et al.*, 2010]. Due to the lack of precise data, we assume here that all faults remain open until the present day. Group 1 of deeply rooted faults has an assigned constant permeability of 1 log (mD) (10^{-15} m^2) whereas the group 2 faults permeability has a value of 2 log (mD) (10^{-14} m^2). An important parameter describing the ability of petroleum or gas to enter the fault already occupied with a fluid (water) is the capillary entry pressure (CEP). Temperature and pressure-dependent interfacial tensions between an already existing phase (e.g., pore fluid) and an invading phase (e.g., oil and gas) are commonly used from reference databases based on lithologies (pore throat radius) and phase properties (e.g., density). It is beyond the scope of this study to evaluate in detail capillary entry pressures for each fault present in the model; therefore, CEPs for both groups of faults are defined with a constant value of 0.01 MPa representing an average value for the present lithology and geological setting [*Hantschel and Kauerauf*, 2009]. Additionally, to explore the possibility of deep-rooted faults being closed and not facilitating hydrocarbon flux, we have performed a sensitivity run assuming the above conditions. The results of this run can be found in supporting information Figure S2.

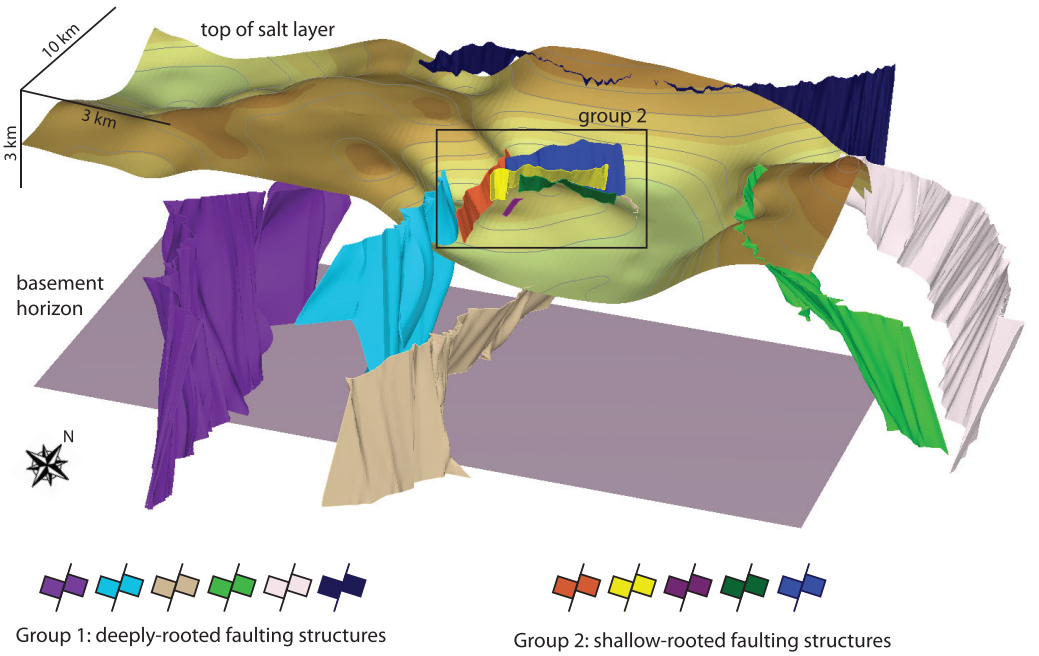

Figure 6. Location of faulting structures interpreted within the modeling domain from seismic data. Horizons representing the top of the salt (upper horizon) and the basement (lower horizon) are shown. Group 1 (left side of the legend) represents deeply rooted structures associated with large-scale remobilization of salt occurring primarily at the edge of the modeling domain. Group 2 represents shallow structures developing at the top of salt domes. They serve as high-permeability pathways for focused gas migration (gas phase collected at the local topographic high underneath the salt layer) and facilitate the transport of gas into the GHSZ.

3.5. Boundary Conditions

According to the model of *McKenzie* [1978], the extent of basal heat flow affecting the heat flow in a sedimentary basin mainly depends on rift-extensional events (basin formation) and the following subsidence due to lithosphere contraction and cooling. Based on the structural evolution of the Gulf of Mexico basin presented by *Sawyer et al*. [1991], we have assumed a syn-rifting phase occurring from 210 to 170 Ma with high heat flow values (locally up to about 88 mW/m^2 at 170 Ma when the Pangaea breakup and the subsequent separation of North and South America occurred, Figure 7) followed by a postrifting phase until present day when the heat flow has reached a modern value of about 42 mW/m^2 [*Nagihara et al*., 1992]. Basin subsidence in time and the above crustal parameters were used to calculate β-stretching factors and create 2-D surface maps of paleo-heat flow at every event predicted in the modeling history. These β values calculated from the 2-D McKenzie crustal model [*Jarvis and McKenzie*, 1980; *McKenzie*, 1978] are similar to regional data from *Sawyer et al*. [1991] that are representative for the region. This data-model conformity supports the validity of the paleo-heat flow trends applied in the model (Figure 7).

The bottom water temperature used as upper boundary condition was assumed to be constant and equal to 4°C over the entire modeling period. An additional modeling scenario assuming bottom water temperature variations based on the study of *Wygrala* [1989] has been incorporated into supporting information Figure S1. Moreover, high sedimentation rates during the Neogene (common for this part of the Gulf of Mexico) affect the thermal history of the basin as they are able to "consume" a large portion of lithospheric heat. On the other hand, coarse clastic material deposited at high rate contains relatively high concentrations of radiogenic elements which lead to an increase of heat in the overall balance. To account for this additional heat production, radioactive decay was included in our modeling study employing average activities of uranium, thorium, and potassium for each lithological facies recognized in the region.

Sea level changes in the history of the northern Gulf of Mexico, mostly driven by plate tectonics, reached up to hundreds of meters until it achieved a relatively stagnant period after the initial 10 Ma of evolution. The paleo-water depth trend used in the modeling study (Figure 7) resulted from a compilation of data from various sources of a different time resolution starting from 165 Ma up to the present day [*Alegret and Thomas*, 2005; *Davis*, 2011; *Miller et al*., 2005; *Salvador*, 1991; *Schroeder et al*., 1995; *Simms et al*., 2009; *Wright*

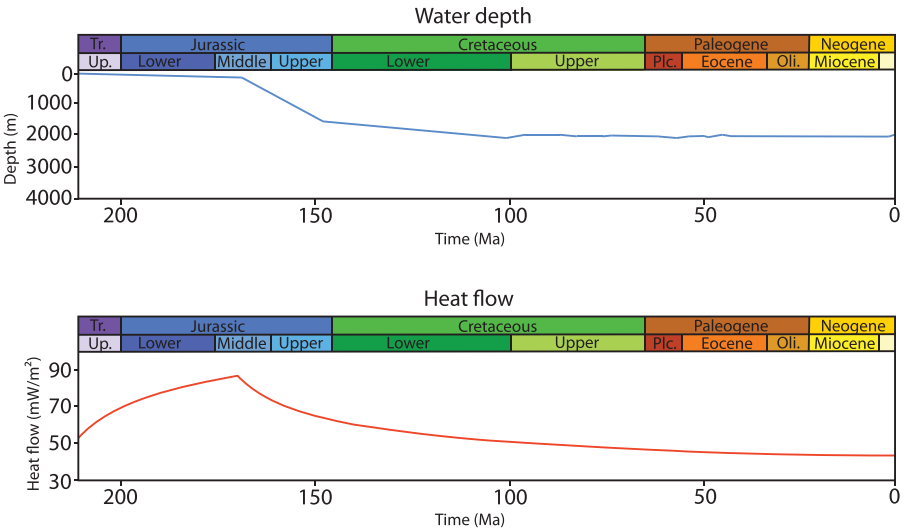

Figure 7. (top) Paleo-water depth and (bottom) paleo-heat flow trends used in the modeling study. Water depth data were implemented after *Alegret and Thomas* [2005], *Davis* [2011], *Miller et al.* [2005], *Salvador* [1991], *Schroeder et al.* [1995], *Simms et al.* [2009], and *Wright et al.* [2005], whereas the heat flow trend shown here represents the average trend of values taken from the precise 2-D maps calculated from the McKenzie crustal rifting model [*Jarvis and McKenzie*, 1980; *McKenzie*, 1978] and assigned separately to each modeled event (e.g., layer deposition) over the history of the basin.

et al., 2005] based on paleo-basin reconstruction, oxygen isotope data, as well as interglacial and glacial shoreline locations. Due to sparse data on Jurassic or Cretaceous periods, some interpolations, especially for the older (>60 Ma) systems, were unavoidable. For the purpose of this study, basin sides were assumed to be open for the entire modeling period allowing an unlimited migration (outflow) of the pore space-filling components. This solution was chosen after performing the test run with closed basin sides (results available in supporting information Figure S7), which resulted in the enhanced outflow migration through the basin top. The overall hydrocarbon losses in the "open" versus "closed" sides runs are about 19 and 16.5 Gt, respectively.

3.6. Simulation

Final simulation runs as well as preliminary test runs were performed on eight CPU work station in a parallel-run mode using a computing facility of Statoil's infrastructure. The model comprises of ~3.20

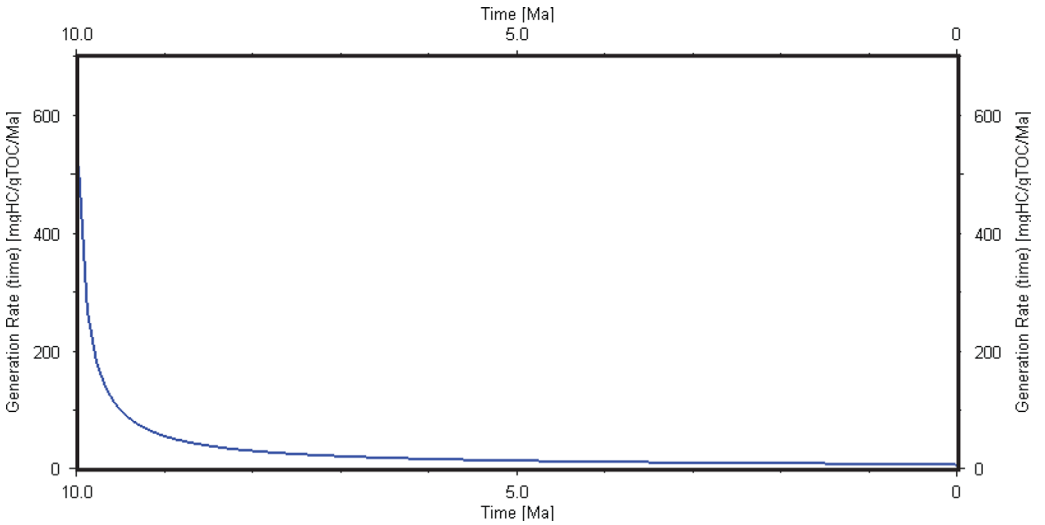

Figure 8. In situ biogenic methane formation according to Middelburg's rate law [*Middelburg*, 1989]. This example plot was generated by assuming an HI = 100 mg HC/g TOC, a burial depth of 1 km, a sedimentation rate of 300 m/Ma, and a deposition start at 10 Ma.

million elements. Simulations contained a total of 241 separate events. The maximum time step of each event (e.g., sedimentary layer deposition) was limited to $\leq$10 Ma. Sedimentary layer were automatically split into thinner packages fulfilling the time step requirements.

3.7. Migration Method

Modeling of multiphase fluid flow in a basin-scale numerical domain containing both low-permeability (e.g., uniform fine-grain lithology) and high-permeability pathways (e.g., faults) is challenging. Fluid, oil, and gas flow in the low-permeability regions are typically computed according to Darcy's law when the flow velocity of the phase remains rather slow. On the other hand, numerical stability of such solutions requires small time steps that increase the overall computational time. To accelerate the numerical simulation in the presence of high-permeability regions experiencing rapid fluid flow, a flow path analysis method is introduced [*Hantschel and Kauerauf*, 2009] which is based on the geometric property of the domain and the preferred flow direction (vertical upward migration). This approach allows for relatively fast and accurate modeling of, e.g., high-buoyancy or petroleum phases and components migration on geological time scales.

Due to high complexity of the 3-D modeling domain presented in this study containing both low and high-permeability regions, we have decided to use the Hybrid method of migration introduced by *Hantschel et al*. [2000] and incorporated into the PetroMod^{TM} software package. The main advantage of this method is the ability to recognize both kinds of domains representing distinct migration efficiency and perform a division of modeling domain prior to the simulation run. In this case, regions recognized as high-permeability structures are faults and reservoirs with a permeability of $>$2.01 log (mD) at 30% porosity. In these regions the flow path analysis method is applied while a Darcy's migration formulation was used to compute the pore fluid and gas migration in the low-permeability domain.

3.8. Simulation of Gas Hydrate Formation

Gas hydrates in the model are allowed to form from both dissolved and free methane gas. Methane diffusion in the pore water is calculated from a temperature-dependent formulation [*Hantschel and Kauerauf*, 2009]. Gas hydrate formation is instantaneous and not kinetically controlled, i.e., the entire methane pool entering the GHSZ and exceeding the CH_4 solubility limit is immediately trapped as gas hydrate. The formation of gas hydrates in the model has an important impact on sediment porosity and permeability as it blocks the potential flow paths for migrating phases (e.g. oil, water, and gas). Multiphase migration in regions recognized as "low-permeability" (section 3.7) follows the Darcy's flow formulation with pore water considered to be a wetting phase (i.e., covering sediments grains with a small water film). A critical (residual) saturation value was introduced for each of the phases (oil, water, and gas) in order to define a saturation threshold at which each phase becomes mobile (5 vol % for water, 3 vol % for oil, and 1 vol % for gas). The choice of low critical saturations of gas are enhancing gas phase migration potential and allow relatively small sizes of bubbles to migrate.

3.9. Gas Hydrate Formation by Organic Matter Biodegradation

As stated above, biogenic methane formation is modeled by using a simple kinetic rate law [*Middelburg*, 1989] relating the reactivity of organic material (R) to its depositional age: $R = 0.16\ (a_0 + z/v)^{-0.95}$, where R is the reaction rate in 1/s, a_0 is the age of the organic carbon in s, z is the burial depth in m, and v is the sedimentation rate in m/s. This formulation requires TOC and HI values as well as sediment age as input parameters which are automatically extracted during basin reconstruction simulation. The HI parameter is used to calculate the generation potential of biogenic methane. Biogenic methane formed is furthermore allowed to diffuse in pore fluids and form gas hydrates within the GHSZ according to local equilibrium conditions. Shallow gas found within Pleistocene layers of the Green Canyon region is mainly formed by biogenic in situ production [*Lorenson et al*., 2008; *Sassen et al*., 2003] due to high Cenozoic rates of sedimentation and large TOC input [*Hutchinson et al*., 2011]. We have introduced in situ biogenic gas formation in all sedimentary layers above the salt (Pliocene and Pleistocene) with a constant initial TOC value of 1 wt % and constant initial HI of 100 mg HC/g TOC, which is in accordance to DSDP data from Site 96 [*Kennicutt et al*., 1985, 1986] and a typical average value acceptable for this kind of marine setting [*Frye*, 2008]. Additionally, biogenic methane formation was modeled (1) throughout Lower Cretaceous to Upper Miocene sediments assuming initial TOC values from 0.8 wt % (e.g., Upper Cretaceous marls) to 1.6 wt % (e.g., Wilcox formation, Paleocene, and Eocene) and initial HI values from 100 mg HC/g TOC to 220 mg HC/g TOC, accordingly, and (2) in the three source rocks present in the region according to the reported initial TOC and HI values (see

Table 1). Moreover, sensitivity analyzes on the initial TOC input available for biodegradation in the Pleistocene layers were performed and the results are available in supporting information Figure S6.

3.10. Gas Hydrate Recycling Process

Rapid sedimentation and burial of prominent gas hydrate accumulations located close to the base of the GHSZ might lead to fast gas hydrate decomposition into the free-gas phase [*Kvenvolden and Barnard*, 1983]. Due to high gas buoyancy and large volumes of instantaneously produced gas, methane might be transported further upward into the overlying GHSZ. Consequent recharge of methane gas from decomposing gas hydrates might lead to significant gas hydrate saturations situated directly at the base of the GHSZ. In principle, the recycling process may occur in any setting. However, it is probably necessary to initiate the process by an injection of methane gas into the gas hydrate stability zone. This priming has to elevate the gas hydrate saturation beyond a threshold value that allows for gas migration when gas hydrate is buried below the base of the GHSZ where it dissociates to form free gas and water. According to the model formulation, the critical gas saturation beyond which the free gas released from hydrate can rise and enter the throats of pores filled with water and hydrate equals to 1 vol %.

3.11. Model Limitations

Due to a lack of data, some model parameters were assumed to be constant over time and space. This applies to the bottom water temperature, the salinity of pore fluids and bottom waters, and the pore entry pressure of faults. Faults introduced in the model as high-permeable pathways are open during their entire presence and allow for a rapid fluid and gas ascent unless they are blocked by gas hydrate formation. Precise timing of, potentially, multiple events of fault reopening and closure might affect the rate of methane transport toward the GHSZ. However, due to lack of reliable data on fault properties evolution in time, we have decided to keep these parameters constant. An additional test run assuming impermeable deep-rooted faults was performed and the results are available in supporting information Figure S2 and Table S1. Because of time step limitations, it was not possible to impose short-term changes in boundary conditions such as sea level changes induced by late Quaternary climate change. Anaerobic oxidation of methane (AOM) was not considered due to software limitations. Therefore, gas hydrate concentrations in the uppermost sedimentary layers (up to about 50 m) are likely overestimated. Due to two-component hydrocarbon generation kinetics used in the modeling study (oil and thermogenic methane gas) and software limitations (the GHSZ calculations provided for only structure I gas hydrates), it was not possible to fully explore a potential presence of structure II gas hydrates and the vertical extent of the corresponding stability zone even though structure II gas hydrates are present in the Gulf of Mexico [*Sassen and Macdonald*, 1994; *Sassen et al*., 2001]. The model does not account for the kinetically possible coexistence of the gas hydrate and free-gas phases within the GHSZ. All methane is immediately trapped as gas hydrate when it enters the stability zone.

4. Results

4.1. Burial History

The burial history of the basin extracted for the nearby JIP Leg II drill wells is shown in Figure 9. The upper plot presents the sediment deposition over the entire modeling period (210 Ma to present) whereas the lower plot focuses on the most recent Neogene sedimentation (23 Ma to present) emphasizing Plio-Pleistocene depositional periods characterized by very large amounts of clastic material delivered to the Green Canyon area mainly from NW direction. Due to high sedimentation rates and changes in lithology within the Miocene unit, significant overpressures were recognized being consistent with data reported by *Piggott and Pulham* [1993]. These overpressures result in an enhanced hydrocarbon migration potential within the deeper part of the sedimentary column and probable development of local fractures acting as high-permeable conduits transporting petroleum components directly into the intrasalt minibasins.

4.2. Source Rock Productivity and Hydrocarbon Generation

Upper Jurassic and mid-Cretaceous organic-rich deposits considered in the modeling study are fully mature and productive as shown in Figure 10. Hydrocarbon generation at the primary Tithonian source rock started about 140 Ma ago for oil and thermogenic gas components and about 130 Ma ago for biogenic methane (see Figure 10a). The Tithonian source rock reached its productivity peak during the Lower Cretaceous with

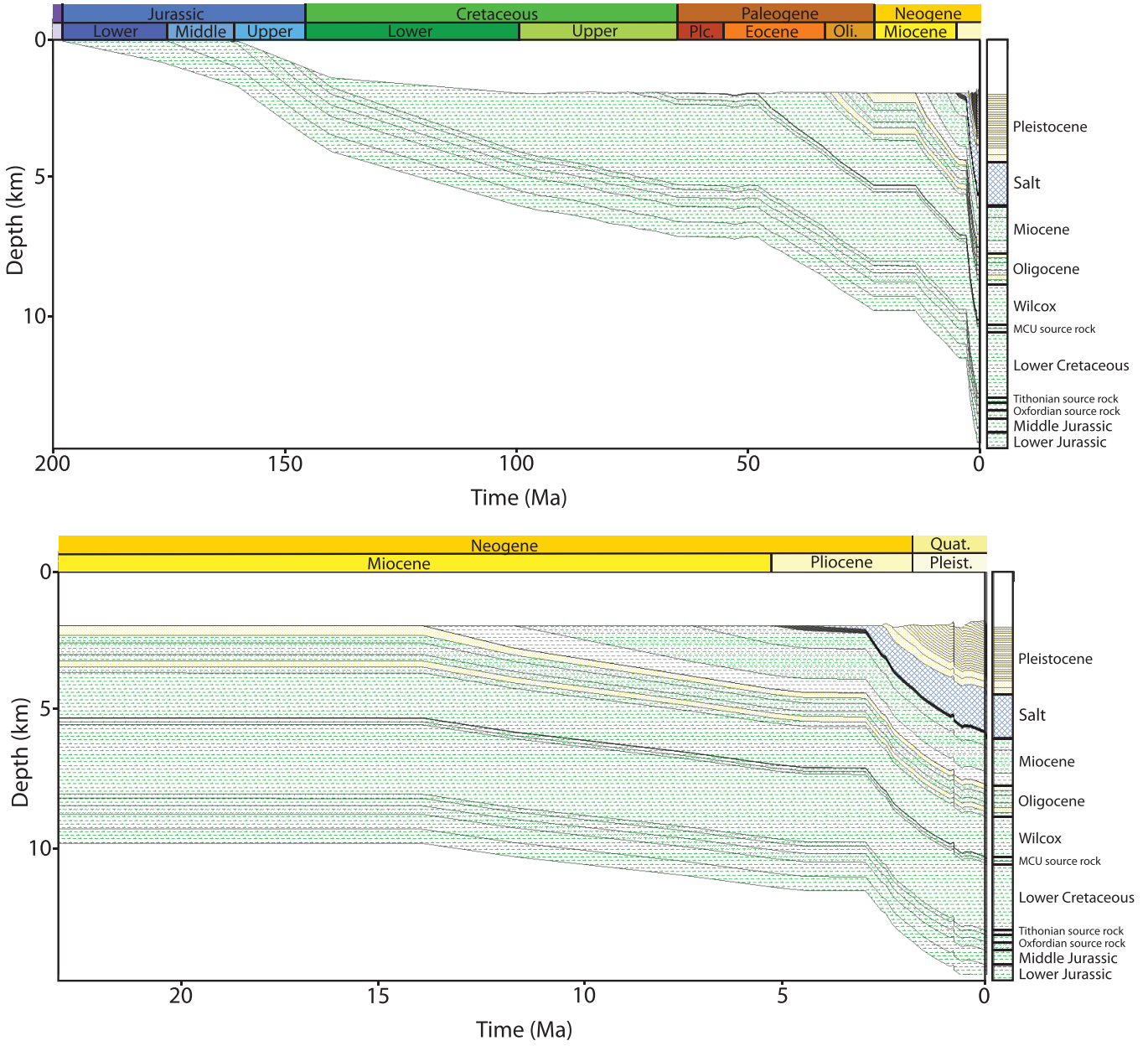

Figure 9. Burial history plot (upper pane: 210 Ma-present, lower pane: 23-present) extracted for the JIP Leg II drill site location showing the most important sediment packages deposited in the history of the basin. Lower panel represents a close-up on the most recent burial history emphasizing the presence of high sedimentation rates starting in the late Miocene up to the present day.

a petroleum mass generation of about 1500 Mt for oil and 1200 Mt for thermogenic methane (see Figure 10d) and the total thermogenic gas production of 1608 Mt. These findings agree with previous estimates of total petroleum components generated over the productivity peak [*Cathles*, 2004; *Cole et al.*, 2001]. The Upper Jurassic source rock of Oxfordian age remained in a productive stage since about 135 Ma (oil component) and 150 Ma (thermogenic methane component) (see Figure 10b) with a productivity peak of about 380 Mt of oil and 30 Mt of thermogenic gas at about 135 Ma until 100 Ma ago (see Figure 10e) and the total thermogenic gas production of 158 Mt. Most likely, Tithonian and Oxfordian source rocks are currently in the postproductivity phase. The Mid-Cretaceous MCU source rock, which is the youngest one present in the study, seems to be productive since about 40 Ma ago (oil component) and 68 Ma (thermogenic gas component) with productivity peak starting at about 62 Ma for thermogenic gas and 40 Ma for oil (see Figure 10c)

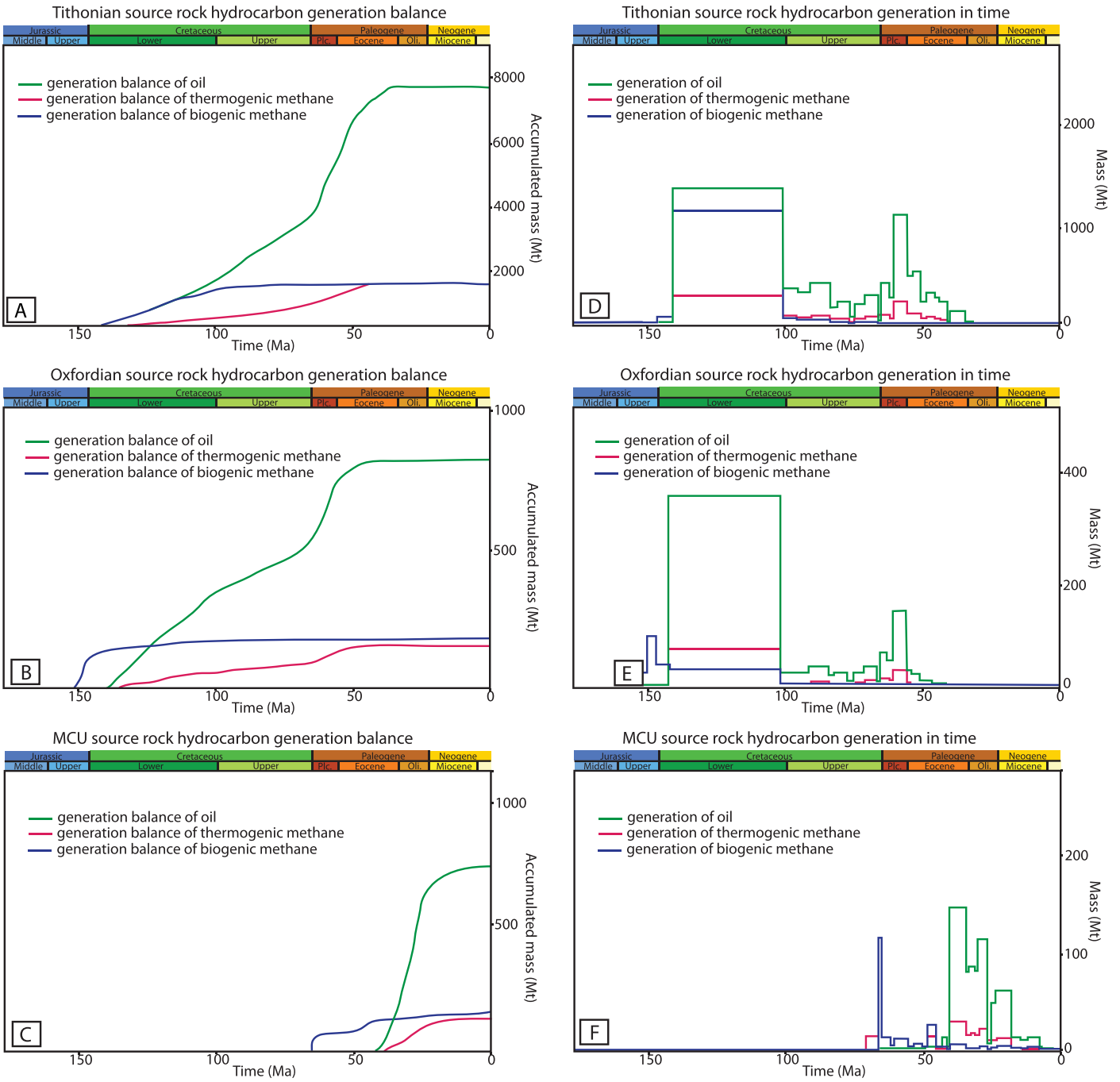

Figure 10. (left) Cumulative generation balance for hydrocarbon components (oil, thermogenic methane, and biogenic methane) for (a) Tithonian, (b) Oxfordian, and (c) MCU source rocks. Generation balance stands for total (accumulated) sum of HC generated due to primary + secondary cracking – components consumed by secondary cracking. (right) Generation of mass (Mt) of oil, thermogenic methane, and biogenic methane integrated over time intervals (simulation "events") indicated by the width of individual bins for (d) Tithonian, (e) Oxfordian, and (f) MCU source rocks.

and the total thermogenic gas production of 136 Mt. A contribution of the MCU at its productivity peak to the total amount of hydrocarbons present in the basin was limited to about 150 Mt of oil and about 115 Mt of thermogenic gas (see Figure 10f). In the following modeling scenarios, we assume that secondary cracking occurs and produces additional volumes of thermogenic methane (see Figure 10). However, total amounts of components produced by this process are small and insignificant in comparison to the overall production generated by primary cracking.

Table 3. Generation Masses and Migration Balance of Biogenic and Thermogenic Methane, and the Total Amount of Present-Day Gas Hydrate Deposits Predicted by the Model

	Biogenic Methane	Thermogenic Methane
Total generation in the model	13,483 Mt	2075 Mt
Total amount migrated out of the model across the top boundary	8328 Mt	1164 Mt
Total amount migrated out of the model across the sides	2669 Mt	314 Mt
Total amount trapped during migration (stagnant phase in shales)	68 Mt	63 Mt
Total amount of gas hydrate present in the model	~3256 Mt of gas hydrate (equals to ~434 Mt of CH_4, ~340 Mt of carbon or, alternatively, ~7×10^{11} m^3 of CH_4 at STP conditions)	

Sensitivity studies assuming variable Tithonian layer thickness (80, 140, and 150 m) as well as the reduction in the initial TOC and HI parameters (TOC equal to 5 wt %, HI to 625 mg HC/g TOC) were performed and are available in supporting information Figures S3–S5. The overall thermogenic methane production from three scenarios ranges from 1130 Mt up to 1714 Mt (see supporting information Table S1), whereas biogenic methane generation remains on the similar level to the reference run (about 13,000 Mt). As a result, a proportionate outflow of methane gas (both thermogenic and biogenic) was observed through the basin top (505–888 Mt for thermogenic and 7649–8147 Mt for biogenic component) and sides of the model (180–241 Mt for thermogenic and 2470–2624 Mt for biogenic component).

As shown in Figure 10, overlapping productivity stages and migration pathways for all three source rocks make a precise analysis of the origin of hydrocarbons somewhat difficult as previously noted by *Cole et al*. [2000, 2001]. As a consequence, thermogenic components that are emitted at gas seeps in the Gulf of Mexico seafloor cannot be attributed to a single deep hydrocarbon source. Moreover, the temperature distribution and maturation potentials of source rocks were modified by high sedimentation rates. Sediments younger than Miocene age present in the region are commonly thought to be thermally immature and thus, not productive [*Nunn and Sassen*, 1986; *Piggott and Pulham*, 1993]. However, in situ microbial production of methane occurs in the Pleistocene layers and significantly contributes to the overall gas hydrate concentration.

A summary of hydrocarbon components generated by primary and secondary cracking, migration losses through the upper model boundary and sides as well as the total amount of gas hydrate accumulated in the sediments is presented in Table 3. The total generation of oil, thermogenic, and biogenic methane amounts to about 26,700 Mt of petroleum (~16,000 Mt of gaseous components only). A clear dominance of the Tithonian source rock productivity among other source rocks is visible as it has generated almost 39% of the overall petroleum mass (about 16% of all gaseous components). Almost all the petroleum generated in the source rocks was expelled (97%) with only a small fraction of methane gas being accumulated within the source rock layers (~330 Mt). Total amount of gas hydrate present within the model boundaries is predicted as ~434 Mt of CH_4 or equivalently, 340 Mt of carbon (see Table 3). Vast majority of generated either thermogenic or biogenic methane is, however, existing in a dissolved or gaseous form within the basin. Total masses as well as rates of thermogenic and biogenic methane lost throughout the modeled basin history are presented in Figure 11.

According to our modeling assumptions, an unlimited outflow of petroleum components could occur across the model sides and through the upper modeling boundary (i.e., the seafloor). The most significant methane loss through the basin sides (about 30 and 800 Mt of thermogenic and biogenic methane gas, respectively) was predicted for the time interval between 2.6 and 2.4 Ma ago (see Figures 11c and 11d, brown lines). This event is strictly correlated with the progressive salt deposition in the region which replaced already existing gas hydrate deposits close to the GHSZ base. Basin subsidence caused by the salt front pushed gas hydrate accumulations downward and outside the stability field which caused their widespread dissociation. Produced free gas was not capable of reentering the GHSZ due to the sealing properties of the salt and migrated sideways along the salt base and left the model domain.

4.3. Gas Hydrate Stability Zone

The temporal evolution of the GHSZ thickness is shown in Figure 12. A relatively thick GHSZ with a large spatial coverage was formed about 160–155 Ma ago (Figures 12a and 12b). No significant changes in the GHSZ thickness can be observed since Tithonian source rock deposition about 145.5 Ma, which suggests

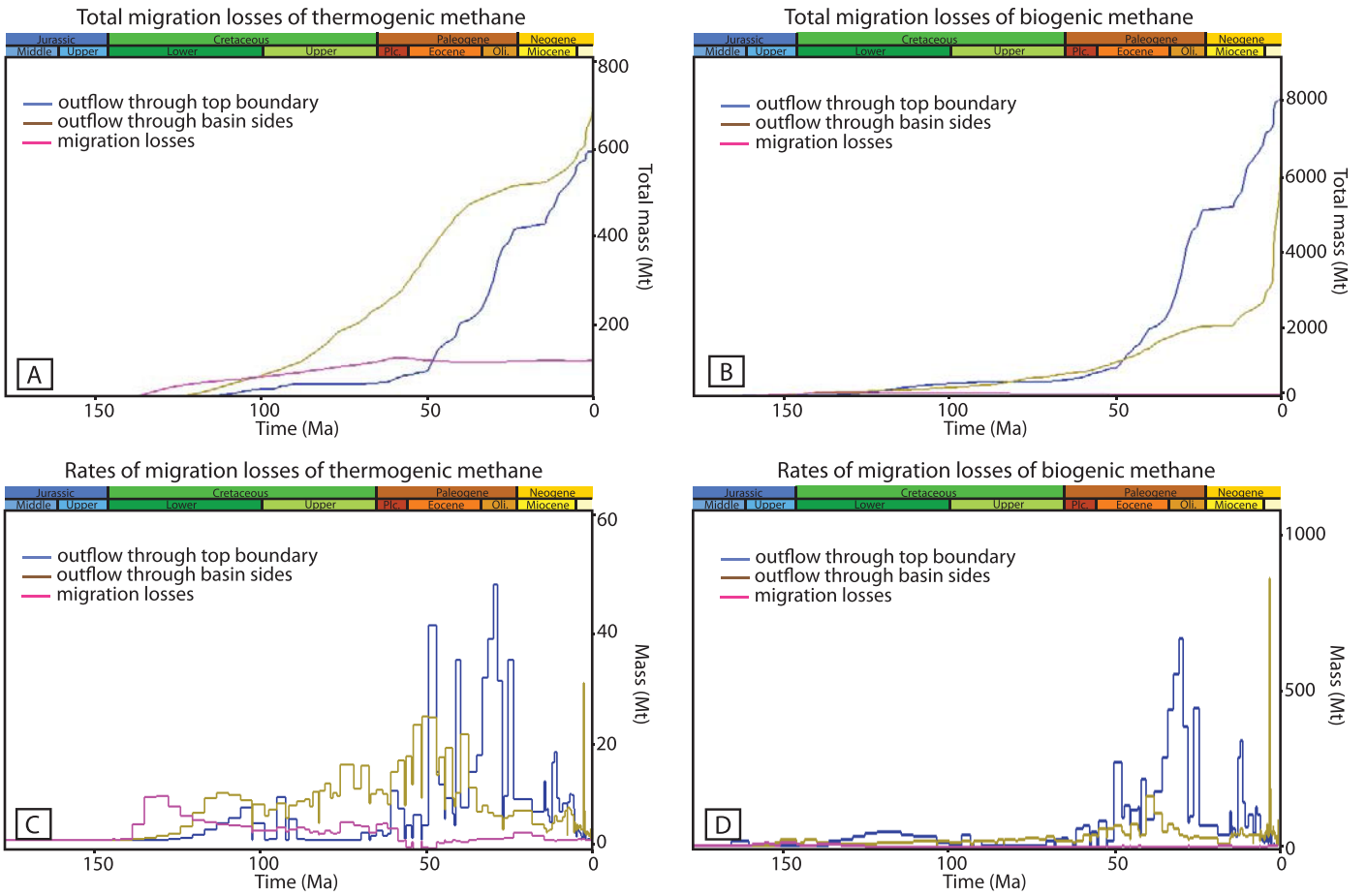

Figure 11. (top) Cumulative amount of (a) thermogenic and (b) biogenic methane that migrated through the top model boundary (i.e., seafloor) (blue lines), through the basin sides (brown lines), and was trapped during the migration process (e.g., accumulated in the shale formation) (violet lines). (bottom) Histogram plots showing the outflow and migration losses of (c) thermogenic and (d) biogenic component integrated over discrete time intervals (simulation "events"). Notice different maximum values on the vertical scale for both components.

that the entire methane pool generated by the two youngest source rocks could be, potentially, trapped within the uppermost gas hydrate reservoir layers since the moment of expulsion and provided that there were efficient migration pathways. However, sensitivity analyzes performed with variable bottom water temperature boundary conditions, included in supporting information Figures S1 and S8, show a significant reduction in the GHSZ thickness from about 145 to 80 Ma ago. As a consequence of warmer environment, additional outflow of methane gas through the basin top shall be expected as it cannot be arrested in the form of a gas hydrate. According to our study, the amount of thermogenic and biogenic methane that might have escaped during that time period was significantly higher (see Table S1 in supporting information). Nevertheless, the overall present-day distribution of gas hydrate deposits seems to be unaffected by the reduction in the GHSZ thickness during the early stage of basin formation. The total amount of gas hydrate predicted for the variable bottom water temperature scenario equals 3086 Mt with thermogenic and biogenic methane generation potential remaining very similar to the reference run (see supporting information Figures S1 and Table S1).

4.4. Gas Hydrate Accumulations

The model predicts a total mass of a present-day gas hydrate accumulations equal to ~3.256 Mt which is equivalent to ~340 Mt of carbon and ~7×10^{11} m^3 of CH_4 at STP conditions. The gas hydrate distribution (from both biogenic and thermogenic sources) within the 3-D modeling domain and a map view of gas hydrates attributed only to a thermogenic origin are presented in Figure 13. Most of the hydrate accumulates in sediment layers close to the base of the GHSZ and locally reaches high saturations up to 80 vol %. The location of prominent gas hydrate deposits next to the GHSZ base seems to be related to two main

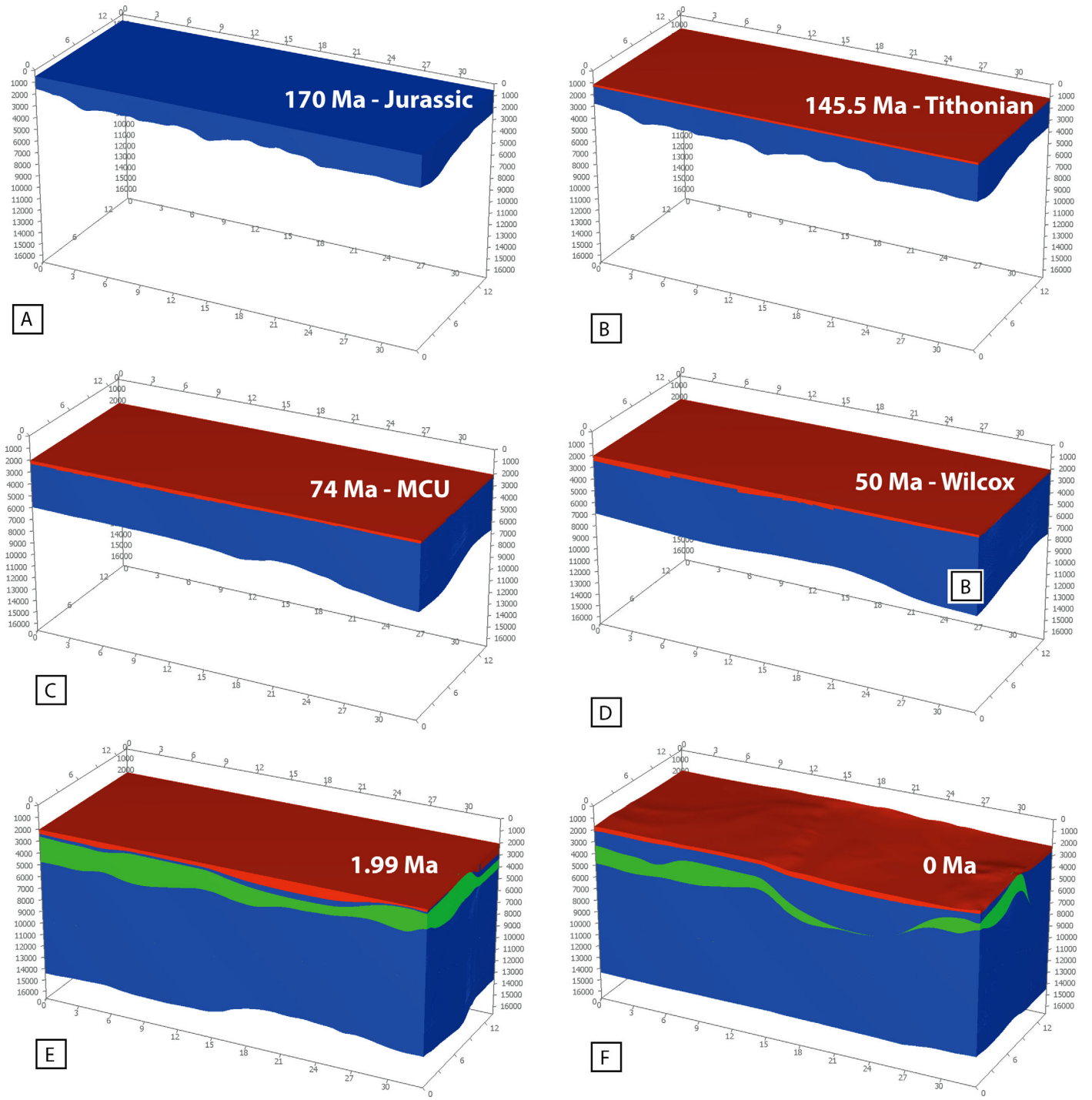

Figure 12. Temporal evolution of the GHSZ highlighted for (a) Jurassic, (b) Tithonian source rock deposition, (c) MCU, and (d) TOC abundant Wilcox formation deposition. Red color indicates presence of the GHSZ while the blue color stands for its absence. Green color in Figures 12e and 12f depicts the location of allochthonous salt deposits to emphasize the evolution of the intrasalt minibasins.

factors: lithological control due to more sandy sediment type available at that depth, and the process of methane gas recycling due to high Neogene sedimentation rates (see more in section 5). Thermogenic gas hydrate deposits are located exclusively at the GHSZ base. Gas hydrate accumulations above 50–60 vol % saturation are most prominent in local depressions that developed between salt rims and where the basin subsidence was the most efficient, e.g., in the NE part of the model domain and the area around JIP drill wells (see Figure 13).

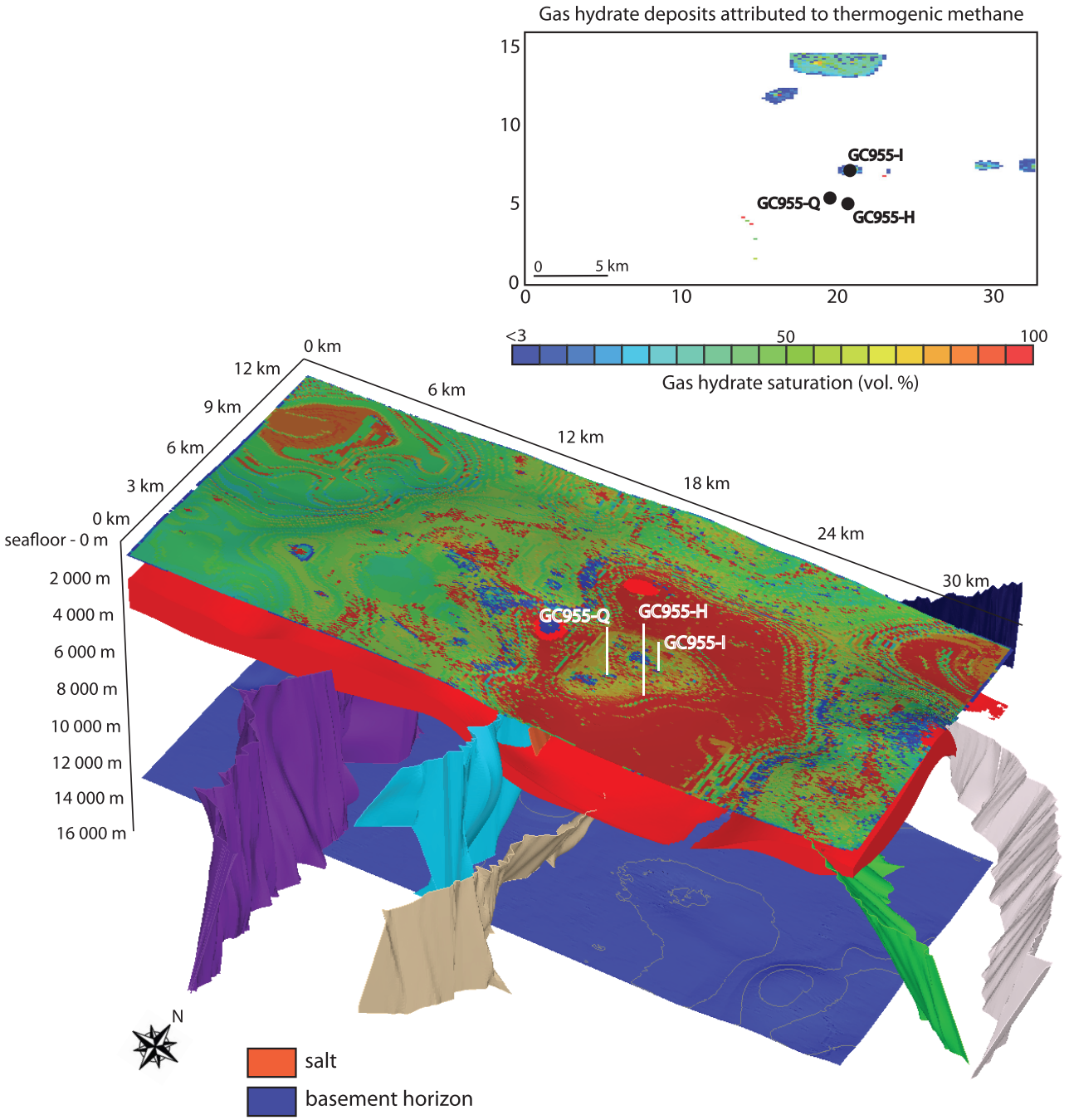

Figure 13. Gas hydrate distribution within Pleistocene sediments of the Green Canyon province (3-D view) presented together with isolated gas hydrate accumulations of exclusively thermogenic methane origin (upper map view). Low gas hydrates concentrations (<3 vol %) commonly observed within uppermost Pleistocene layers are not shown in this figure to keep the clarity of the picture. Therefore, only gas hydrate saturations >3 vol % (regardless of their location) are depicted. Effectively, this 3-D view can be interpreted as gas hydrate saturations at the base of the GHSZ. The salt layer visible in the 3-D view is shown in red, whereas the basement horizons defining the bottom boundary of modeling domain is shown in blue. Interpreted faulting structures are shown here to emphasize the 3-D interplay between fault position and gas hydrate accumulation within the GHSZ.

According to our simulations, a vivid in situ biogenic methane production resulting in abundant gas hydrate deposits in the Pleistocene-Pliocene sediments started about 1.7 Ma ago (see Figure 14 showing the evolution of the gas hydrate deposits in time). However, prior to that age, gas hydrate saturations remained relatively small (10–15 vol % on average) in comparison to the present day. Due to the high gas hydrate saturations (>80 vol %) calculated mostly for low-topographic areas, sediment porosity and permeability are strongly reduced which effectively blocks fluid flow through the pore space and additional methane

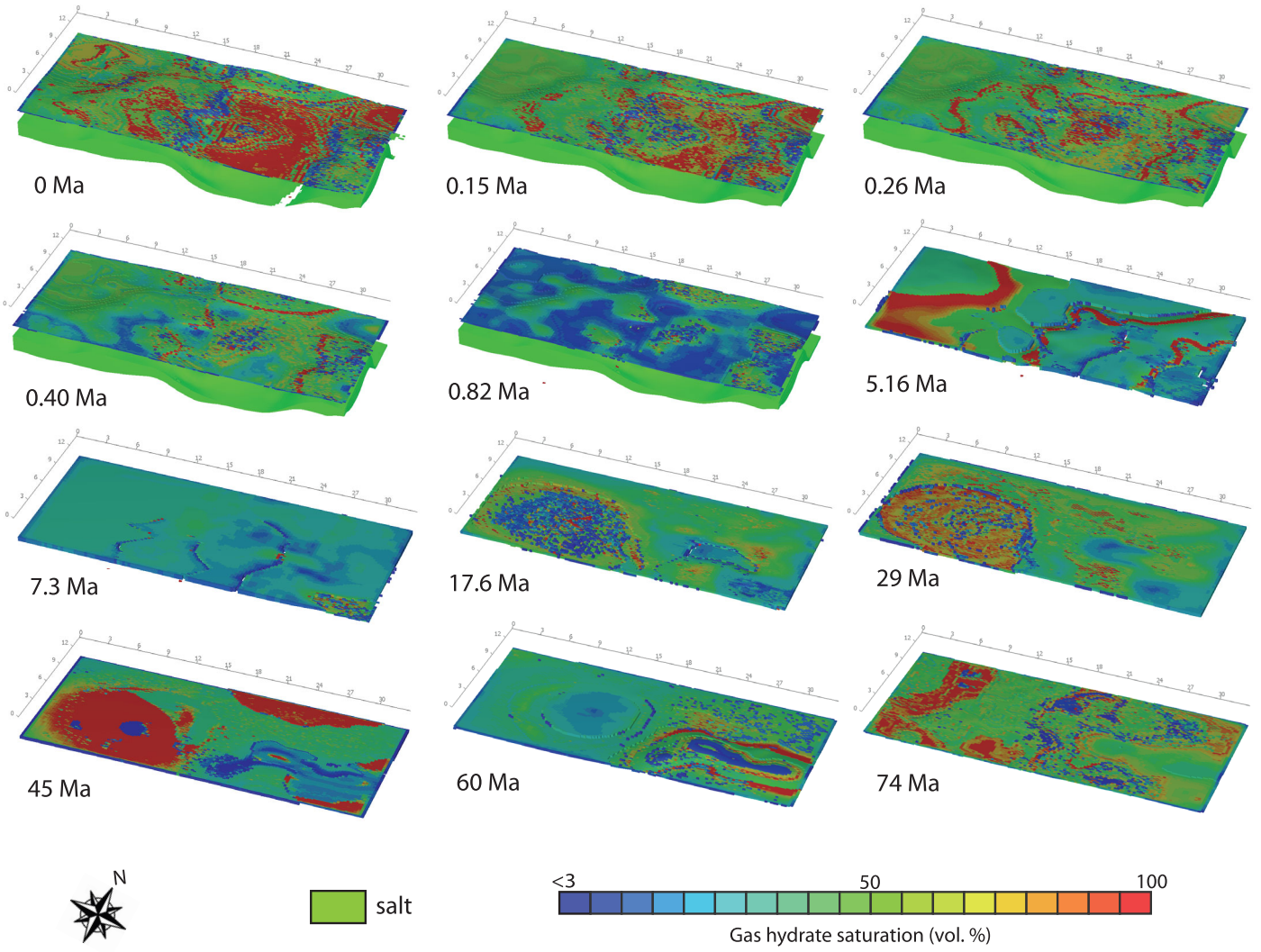

Figure 14. Temporal evolution of gas hydrate deposits. We have chosen the ages of 74, 60, 45, 29, 17.6, 7.3, 5.16, 0.82, 0.4, 0.26, 0.15 Ma, and the present-day state to emphasize the presence of wide-spread gas hydrate accumulations in the history of the basin. According to our simulations, the gas recycling process at the base of the GHSZ occurred for the last ~0.8 Ma and is represented by the figures related to a time frame 0.82–0 Ma.

supply from underlying layers, thereby creating local overpressures to evolve due to the presence of a free-gas phase. These modeled gas hydrate saturations are consistent with findings at the GC955-Q well indicating the presence of free gas directly underneath abundant gas hydrate accumulations located at the base of the GHSZ [*Guerin et al*., 2009; *Hutchinson et al*., 2009; *McConnell et al*., 2010].

Gas hydrate saturations within the uppermost Pleistocene layers (first 300–500 m) are rather low (~1–3 vol %), locally up to 5–8 vol %. This is caused by a limited gas flux from below and strongly decreased porosity at the lower boundary of the GHSZ due to high gas hydrate concentrations. A detailed comparison of modeled gas hydrate concentrations with respect to the well locations (GC955-I, GC955-Q, and GC955-H) is shown in 2-D cross sections in Figure 15 and further discussed in the section 5.

The present-day gas hydrate distribution in the test runs assuming variable source rock parameters does not change with respect to the reference run due to predominant biogenic methane origin. Total amount of gas hydrate present within the model domain and predicted by the sensitivity tests ranges from 3357 to 3400 Mt (see supporting information Table S1). To evaluate the importance of the initial TOC input within Pleistocene layers on the total gas hydrate deposits, we have performed a sensitivity run assuming a reduction in the organic matter available for biodegradation to 0.7 wt %. The results of that run can be found in supporting information Figure S6 and Table S1. The total amount of gas hydrate predicted by this

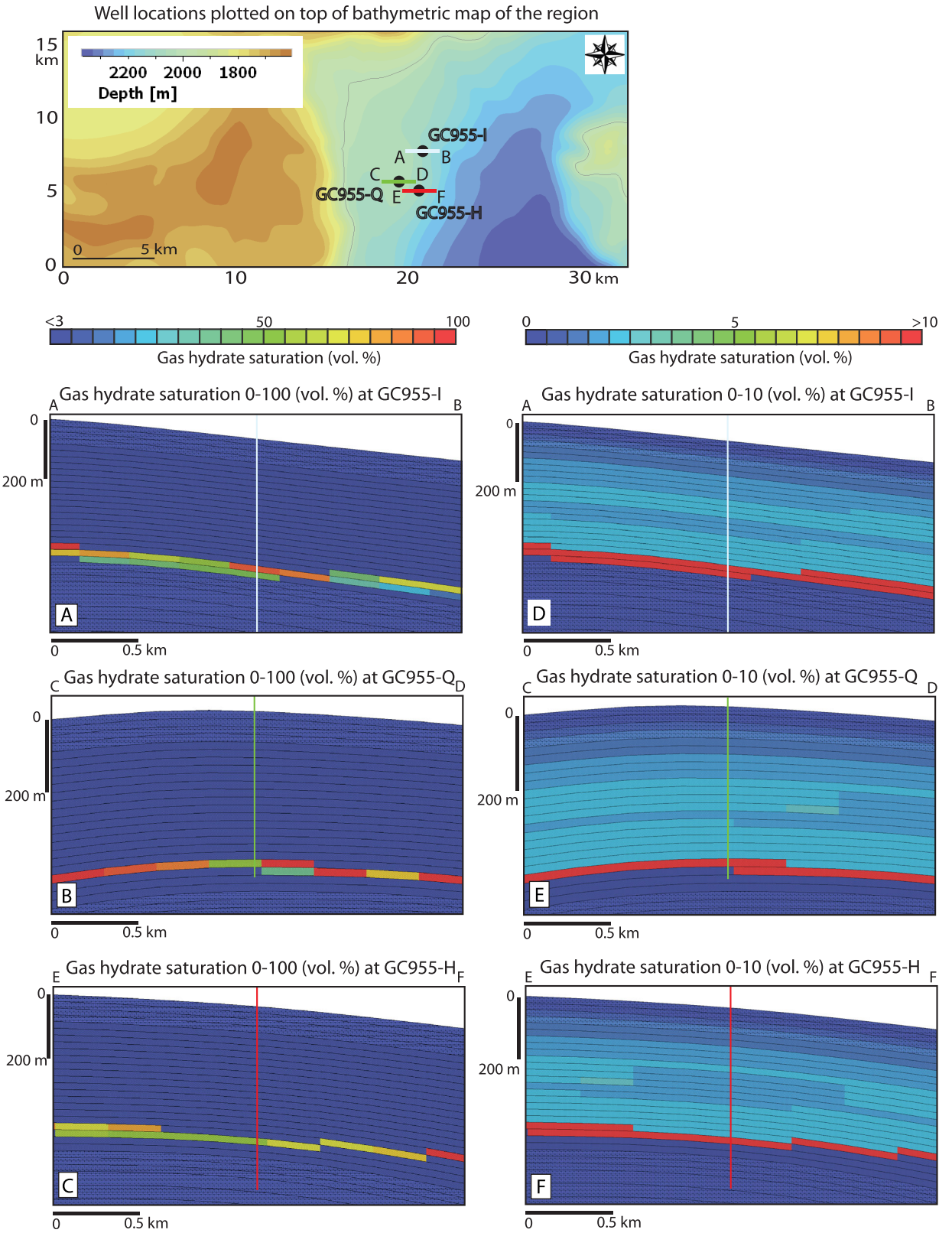

Figure 15. (top) A bathymetric contour map showing the location of the well GC955-H, GC955-I, and GC955-Q with indication for three 2 km wide cross sections along JIP wells. (a–c) Gas hydrate concentrations above 3 vol %. Continuous horizon with high (here >10 vol %, in reality about 80–100 vol %) is clearly visible for each well and corresponds to the base of gas hydrate stability zone. (d–f) Gas hydrate concentrations limited to 10 vol % to emphasize local variations in low gas hydrate concentrations due to biogenic methane production.

simulation equals 2786 Mt (–14.5% with respect to the reference run). As expected, biogenic methane generation is significantly lower than in the reference run (12,720 Mt), whereas thermogenic methane generation amounts to 2074 Mt (supporting information Table S1), closely to the reference run (Table 3). The present-day gas hydrate distribution in the model resulting from the low initial TOC simulation exhibits general similarities; however, mainly the low-topographic regions (e.g., NW and NE) are predicted to host less prominent hydrate saturations oscillating around 45 vol %. Especially, the NE depression situated next to the Green Knoll feature is expected to have no more than 10–15 vol % of gas hydrate situated in the outer rim of the depression.

5. Discussion

Assuming a global inventory of gas hydrates in marine sediments of ∼1000 Gt C [*Burwicz et al*., 2011; *Pinero et al*., 2013; *Wallmann et al*., 2012], the small area of the Green Canyon, investigated in our study, may, thus, contribute about 0.03% to the global inventory. Taking into account some uncertainties of the above numbers and using the *Milkov*'s [2004] range of 500–2500 Gt of C as a total gas hydrate estimate, the investigated Green Canyon area would contribute about 0.01–0.07% to the global deposits. Considering the size of the model domain of about 448 km^2, an average depth-integrated gas hydrate deposits amounts to 0.75 Mt C/km^2 which is equivalent to 1.56 billion cubic meters (BCM)/km^2. Similar predictions obtained with different method (transfer function integrating well and seismic data) on the GC955 resource potential assume the gas hydrate density of ∼1.8 BCM/km^2 [*Frye et al*., 2012]. More conservative gas hydrate estimates made by the same authors for the Terrebonne Basin (northern Gulf of Mexico) assume 1.183 BCM/km^2. Comparatively, the test run assuming lower TOC content (0.7 wt %; see supporting information Figure S6 and Table S1) available for biodegradation in the Pleistocene layers predicts gas hydrate density of about 1.352 BCM/km^2. Assuming that the vast majority of global gas hydrate deposits (estimated total value of ∼1000 Gt C) is located within continental margins covering ∼57,600,000 km^2 of the Earth's surface [*Vion and Menot*, 2009], the average gas hydrate concentration equals ∼0.02 Mt C/km^2. Therefore, an average of predicted gas hydrate concentration at the Green Canyon is about 40 times higher than a rough estimate of the continental margin gas hydrate.

High gas hydrate saturations currently present at the base of the GHSZ are commonly attributed to the presence of sand-dominated lithology. However, a progressive increase of gas hydrate saturations up to >80 vol % close to the base of the GHSZ that has been modeled for the last 0.82 Ma can be explained in part by very high Neogene sedimentation rates which caused a rapid subsidence of the basin and, consequently, translation of the lower GHSZ boundary upward and toward the seafloor. As a result of newly deposited thick sediment packages on top of local depressions, relatively deep secondary intrasalt minibasins developed. Gas hydrate deposits located at the base of the GHSZ were subsequently buried deeper and moved outside the stability field causing their dissociation and the formation of free gas which, in turn, started to migrate upward and reentered the stability zone causing a significant increase in gas hydrate saturations at those depths. Time scales of methane gas migration with respect to the burial rates of sediments are much faster and thus, an instantaneous recharge of gas hydrate deposits at the base of the GHSZ occurred. We attribute this process of recycling between gas hydrate and free gas at the base of stability field to the extreme Neogene sediment load (compare Figure 14, ages between 0.82 Ma and the present day) and conclude that it is the major reason for the occurrence of wide-spread high concentrations of gas hydrate in the local topographic troughs. According to our simulations, an initial gas hydrate saturation of 8–10 vol % is required to initiate an effective methane gas recycling process at the base of the GHSZ. In case of regions with lower gas hydrate saturations (<8 vol %), methane recycling was progressing slower despite comparable sedimentation rates.

According to the drilling reports [*Guerin et al*., 2009; *Hutchinson et al*., 2009; *McConnell et al*., 2010], borehole GC955-I encounters the base of the GHSZ at a depth of 444 mbsf, and the borehole GC955-H at a depth of 450 mbsf which is in good agreement with our predictions of the base of the GHSZ ranging between 439 and 458 mbsf (GC955-I) and between 435 and 459 mbsf (GC955-H). The deepest sediment depth drilled by well GC955-Q most likely did not reach the lower boundary of the GHSZ [*Collett et al*., 2012]; however, the base of the GHSZ base was estimated to be at the depth of 461 mbsf which is in accordance with our numerical predictions (i.e., 445–467 mbsf). Gas hydrate saturations estimated from the LWD method at the

base of the GHSZ vary up to 50 vol % for well GC955-I (depth interval of 420–440 mbsf), around 50–80 vol % for well GC955-H (depth interval of 412–450 mbsf), and around 20–40 vol % (locally up to 75 vol %) for well GC955-Q (depth interval of 414–442 mbsf). Our numerical simulations suggest very similar gas hydrate distribution and predict ~50 vol % at the base of GHSZ and ~86 vol % in the upper adjacent horizon (depth interval of 419–458 mbsf) for well GC955-I (see Figure 15a), ~50 vol % at the base and 40–80 vol % in two overlying horizons (depth interval of 412–467 mbsf) for a well GC955-Q (see Figure 15b), and 50–60 vol % at the base of the GHSZ (depth interval of 435–459 mbsf) for well GC955-H (see Figure 15c). Moreover, we were able to identify higher gas hydrate saturations within layers characterized by a higher percentage of a coarse-grained material (Figures 15d–15f). Besides prominent gas hydrate concentrations at the base of the GHSZ reported for all three wells, additional hydrate-bearing horizons were identified by sediment resistivity analysis for at least two wells: GC955-I at the depths of 365–442 mbsf (reported as "low saturations"), and GC955-H at the depths of 192–309 mbsf (~5 vol %). These findings are consistent with our simulations which predict 2–3 vol % saturation of gas hydrates within sediment horizons located in a depth of 355–419 and 209–270 mbsf at well GC955-I (see Figure 15d), and within two depth intervals of 194–218 mbsf (2–3 vol %) and 260–279 mbsf (about 5 vol %) at well GC955-H (see Figure 15f).

6. Conclusions

The northern Gulf of Mexico is an area with a high potential for submarine gas hydrate formation: mature source rocks produce large amounts of hydrocarbon gases, efficient migration pathways exist along fault structures, and paleo channel-levee systems throughout the Neogene sediments provide a perfect reservoir for gas hydrate formation within a thick gas hydrate stability zone of 400–500 m (locally even up to 900 m). Moreover, high rates of sedimentation and strong organic matter supply assure efficient microbial in situ gas production directly within the GHSZ. The presence of gas hydrates in the Green Canyon region was confirmed by JIP Leg II operation which revealed moderate (about 20 vol %) to high (about 80 vol %) gas hydrate concentrations in thick sandy intervals close to the base of the GHSZ.

Our study demonstrates the strength and feasibility of a cutting-edge three-dimensional modeling approach that resolves, for the first time, a natural gas hydrate system in a complex basin scale and produces results that are in good agreement with independent borehole observations. Full basin reconstruction allowed for drawing conclusions on the history of the GHSZ and gas hydrate accumulations in the region. The results of this study were calculated with high spatial precision (locally up to 1 m), thus enabling a direct comparison with drill data and seismic images. The presented study predicts present-day accumulations within the model domain (~448 km^2 of seafloor area) amounting up to about 3256 Mt of gas hydrate which is equivalent to ~340 Mt of carbon in total and to $\sim 7 \times 10^{11}$ m^3 of CH_4 at STP conditions. The average depth-integrated gas hydrate inventory of 0.75 Mt C/km^2 exceeds by a factor of 40 the corresponding average value for continental margins [*Burwicz et al*., 2011; *Pinero et al*., 2013; *Wallmann et al*., 2012].

The general pattern of the simulated gas hydrate distribution (showing high concentrations >80 vol % close to the base of the GHSZ) is primarily caused by the recycling of gas hydrate and free gas at the base of the GHSZ fueled by methane generation from in situ microbial sources and migration of thermogenic methane from great sediment depth. According to our model, the efficient biogenic methane recycling is the main mechanism of concentrating gas hydrate deposits at the base of the GHSZ. Moreover, biogenic methane formation is dominant for recent high sedimentation rates coupled with high POC input. Therefore, the majority of present-day gas hydrates in the area is relatively young and of biogenic rather than of thermogenic origin (see Figure 13). These results are consistent with findings of the JIP Leg II cruise [*Guerin et al*., 2009; *Hutchinson et al*., 2009; *McConnell et al*., 2010].

Our pioneer study shows that basin-scale modeling can be employed to predict gas hydrate accumulation at specific sites where reliable geological data are available. Future applications of this new modeling tool will help to reduce exploration costs and improve estimates of gas hydrate distributions in sedimentary basins. Hence, our study may facilitate the development of gas hydrates as a new unconventional resource of natural gas [*Boswell and Collett*, 2011]. It will also help to better understand the role of gas hydrates in the global carbon cycle [*Wallmann et al*., 2012] and the amplification of global warming by gas hydrate dissociation [*Archer*, 2007; *Biastoch et al*., 2011].

Acknowledgments
This study has been financed by the German gas hydrate program SUGAR (BMBF grant 03G0819A and 03G0856A) and by Statoil ASA, Stavanger, Norway as a joint academia-industry project. The authors are grateful for constructive comments from Matthew Frye and Tim Minshull which greatly improved the manuscript. Data generated by this study can be accessible under request from the first author (eburwicz@geomar.de).

References

Alegret, L., and E. Thomas (2005), Cretaceous/Paleogene boundary bathyal paleo-environments in the central North Pacific (DSDP Site 465), the Northwestern Atlantic (ODP Site 1049), the Gulf of Mexico and the Tethys: The benthic foraminiferal record, *Paleogeogr. Paleoclimatol. Paleoecol.*, *224*, 53–82.

Archer, D. (2007), Methane hydrate stability and anthropogenic climate change, *Biogeosciences*, *4*, 521–544.

Archer, D., and B. A. Buffett (2012), A two-dimensional model of the methane cycle in a sedimentary accretionary wedge, *Biogeosciences*, *9*, 3323–3336.

Archer, D., B. A. Buffett, and P. C. McGuire (2012), A two-dimensional model of the passive coastal margin deep sedimentary carbon and methane cycles, *Biogeosciences*, *9*, 2859–2878.

Athy, L. F. (1930), Density, porosity, and compaction of sedimentary rocks, *AAPG Bull.*, *14*, 1–24.

Baba, K., and A. Katoh (2004), Application of a simulation model for the formation of methane hydrate to the Nankai Trough and the Blake Ridge: Natural examples of two end-member cases, *Resour. Geol.*, *54*, 125–135.

Bhatnagar, G., W. G. Chapman, G. R. Dickens, B. Dugan, and G. J. Hirasaki (2007), Generalization of gas hydrate distribution and saturation in marine sediments by scaling of thermodynamic and transport processes, *Am. J. Sci.*, *307*, 861–900.

Biastoch, A., et al. (2011), Rising Arctic Ocean temperatures cause gas hydrate destabilization and ocean acidification, *Geophys. Res. Lett.*, *38*, L08602, doi:10.1029/2011GL047222.

Bird, D. E., K. Burke, S. A. Hall, and J. F. Casey (2005), Gulf of Mexico tectonic history: Hotspot tracks, crustal boundaries, and early salt distribution, *AAPG Bull.*, *89*, 311–328.

Boswell, R., and T. S. Collett (2011), Current perspectives on gas hydrate resources, *Energy Environ. Sci.*, *4*, 1206–1215.

Boswell, R., T. S. Collett, M. Frye, W. Shedd, D. R. McConnell, and D. Shelander (2012a), Subsurface gas hydrates in the northern Gulf of Mexico, *Mar. Pet. Geol.*, *34*, 4–30.

Boswell, R., M. Frye, D. Shelander, W. Shedd, D. R. McConnelle, and A. Cook (2012b), Architecture of gas-hydrate-bearing sands from Walker Ridge 313, Green Canyon 955, and Alaminos Canyon 21: Northern deepwater Gulf of Mexico, *Mar. Pet. Geol.*, *34*, 134–149.

Burnham, A. K. (1989), A simple kinetic model of petroleum formation and cracking, *Tech. Rep. UCID-21665*, Lawrence Livermore Natl. Lab., Calif, Livermore, Calif.

Burwicz, E. B., L. H. Ruepke, and K. Wallmann (2011), Estimation of the global amount of submarine gas hydrates formed via microbial methane formation based on numerical reaction-transport modeling and a novel parameterization of Holocene sedimentation, *Geochim. Cosmochim. Acta*, *75*, 4562–4576.

Cathles, L. M. (2004), Hydrocarbon generation, migration, and venting in a portion of the offshore Louisiana Gulf of Mexico basin, *Leading Edge*, *23*(8), 760–770.

Chatterjee, S., G. R. Dickens, G. Bhatnagar, W. G. Chapman, B. Dugan, G. T. Snyder, and G. J. Hirasaki (2011), Pore water sulfate, alkalinity, and carbon isotope profiles in shallow sediment above marine gas hydrate systems: A numerical modeling perspective, *J. Geophys. Res.*, *116*, B09103, doi:10.1029/2011JB008290.

Cole, G. A., et al. (2000), Jurassic to lower Cretaceous sourced petroleum system, deepwater to ultradeepwater Gulf of Mexico, offshore Louisiana, *Abstr. Pap. Am. Chem. Soc.*, *219*, U690.

Cole, G. A., A. Yu, F. Peel, C. E. Taylor, R. Requejo, J. DeVay, J. M. Brooks, B. Bernard, J. Zumberge, and S. Brown (2001), The deepwater GoM petroleum system: Insights from piston coring, defining seepage, anomalies, and background, paper presented at 21st Annual GCSSEPM Foundation Research Conference, GCSSEPM Found., Houston, Tex.

Collett, T. S., W. L. Myung, M. V. Zyrianova, S. A. Mrozewski, G. Guerin, A. E. Cook, and D. Goldberg (2012), Gulf of Mexico gas hydrate joint industry project Leg II logging-while-drilling data acquisition and analysis, *Mar. Pet. Geol.*, *34*, 41–61.

Davie, M. K., and B. A. Buffett (2001), A numerical model for the formation of gas hydrate below the seafloor, *J. Geophys. Res.*, *106*, 497–514.

Davie, M. K., and B. A. Buffett (2003), Sources of methane for marine gas hydrate: Inferences from a comparison of observations and numerical models, *Earth Planet. Sci. Lett.*, *206*, 51–63.

Davis, R. A., Jr. (2011), *Sea-Level Change in the Gulf of Mexico*, Texas A&M Univ. Press, College Station.

Diegel, E. A., D. C. Schuster, J. F. Karlo, R. C. Shoup, and P. R. Tauvers (1995), Cenozoic structural evolution and tectono-stratigraphic framework of the Northern Gulf coast continental margin, in *Salt Tectonics: A Global Perspective, AAPG Mem*. 65, edited by M. P. A. Jackson, D. G. Roberts, and S. Snelson, pp. 109–151.

Egeberg, P. K., and G. R. Dickens (1999), Thermodynamic and pore water halogen constraints on gas hydrate distribution at ODP Site 997 (Blake Ridge), *Chem. Geol.*, *153*, 53–79.

Frye, M. (2008), Preliminary evaluation of in-place gas hydrate resources: Gulf of Mexico outer continental shelf, MMS Gulf of Mexico in-place hydrate assessment, U.S. Dep. of the Inter. Miner., Manage. Serv., Resour. Eval. Div.

Frye, M., W. Shedd, and R. Boswell (2012), Gas hydrate resource potential in the Terrebonne Basin, Northern Gulf of Mexico, *Mar. Pet. Geol.*, *34*, 150–168.

Garg, S. K., J. W. Pritchett, A. Katoh, K. Baba, and T. Fujii (2008), A mathematical model for the formation and dissociation of methane hydrates in the marine environment, *J. Geophys. Res.*, *113*, B01201, doi:10.1029/2006JB004768.

Guerin, G., A. Cook, S. Mrozewski, T. Collet, and R. Boswell (2009), Gulf of Mexico gas hydrate joint industry project Leg II: Green Canyon 955 LWD operation and results, in *Proceedings of the Drilling and Scientific Results of the 2009 Gulf of Mexico Gas Hydrate Joint Industry Project Leg II*.

Hantschel, T., and A. I. Kauerauf (2009), *Fundamentals of Basin and Petroleum Systems Modeling*, Springer, Berlin.

Hantschel, T., A. I. Kauerauf, and B. Wygrala (2000), Finite element analysis and ray tracing modeling of petroleum migration, *Mar. Pet. Geol.*, *17*, 815–820.

Hood, K. C., L. M. Wenger, O. P. Gross, and S. C. Harrison (2002), Hydrocarbon systems analysis of the northern Gulf of Mexico: Delineation of hydrocarbon migration pathways using seeps and seismic imaging, in *Surface Exploration Case Histories: Applications of Geochemistry, Magnetics, and Remote Sensing*, *AAPG Stud. Geol. 48, SEG Geophys. Ref. Ser. 11*, edited by D. Schumacher and L. A. LeSchack, pp. 25–40 AAPG, Tulsa, Okla.

Hutchinson, D., et al. (2009), Gulf of Mexico gas hydrate joint industry project Leg II-Green Canyon 955 site selection, in *Proceedings of the Drilling and Scientific Results of the 2009 Gulf of Mexico Gas Hydrate Joint Industry Project Leg II*.

Hutchinson, D., C. Ruppel, H. H. Roberts, R. Carney, and M. Smith (2011), *Gas Hydrates in the Gulf of Mexico*, Texas A&M Univ. Press, College Station.

Jarvis, G. T., and D. P. McKenzie (1980), Sedimentary basin formation with finite extension rates, *Earth Planet. Sci. Lett.*, *48*, 42–52.

Katoh, A., K. Nakayama, K. Baba, and T. Uchida (2000), Model simulation for generation and migration of methane hydrate, *Energy Explor. Exploit.*, *18*, 401–421.
Kennicutt, M. C., J. M. Brooks, T. J. McDonald, and R. C. Pflaum (1985), Nonvolatile organic-matter at sites-565-570, deep-sea drilling project Leg-84, *Initial Rep. Deep Sea Drill. Proj.*, *84*, 705–717.
Kennicutt, M. C., D. A. Defreitas, J. E. Joyce, and J. M. Brooks (1986), Nonvolatile organic-matter in sediments from site-614 to site-623, deep-sea-drilling-project Leg-96, *Initial Rep. Deep Sea Drill. Proj.*, *96*, 747–756.
Kroeger, K. F., A. Plaza-Faverola, P. M. Barnes, and I. A. Pecher (2015), Thermal evolution of the New Zealand Hikurangi subduction margin: Impact on natural gas generation and methane hydrate formation—A model study, *Mar. Pet. Geol.*, *63*, 97–114.
Kvenvolden, K. A., and L. A. Barnard (1983), Hydrates of natural gas in continental margins, *AAPG Mem.*, *34*, 631–640.
Lee, M. W., and T. S. Collett (2012), Pore- and fracture-filling gas hydrate reservoirs in the Gulf of Mexico Gas Hydrate Joint Industry Project Leg II Green Canyon 955 H well, *Mar. Pet. Geol.*, *34*, 62–71.
Lorenson, T. D., G. E. Claypool, and J. A. Dougherty (2008), Natural gas geochemistry of sediments drilled on the 2005 Gulf of Mexico JIP cruise, *Mar. Pet. Geol.*, *25*, 873–883.
McBride, B. C., M. G. Rowan, and P. Weimer (1998), The evolution of allochthonous salt systems, northern Green Canyon and Ewing Bank (offshore Louisiana), northern Gulf of Mexico, *AAPG Bull.*, *82*, 1013–1036.
McConnell, D. (2000), Optimizing deepwater well locations to reduce the risk of shallow water flow, in *Proceedings of Offshore Technology Conference*, vol. 32, pp. 87–97.
McConnell, D. R., et al. (2010), Gulf of Mexico Gas Hydrate Joint Industry Project Leg II: Initial Results from the Green Canyon 955 Site, in Proceedings of the Offshore Technology Conference, May 3–6, Curran Associates, Inc., paper number OTC 20801, Houston, Tex.
McKenzie, D. (1978), Some remarks on development of sedimentary basins, *Earth Planet. Sci. Lett.*, *40*, 25–32.
Middelburg, J. J. (1989), A simple rate model for organic matter decomposition in marine sediments, *Geochim. Cosmochim. Acta*, *53*, 1577–1581.
Milkov, A. V. (2004), Global estimates of hydrate-bound gas in marine sediments: How much is really out there?, *Earth Sci. Rev.*, *66*, 183–197.
Milkov, A. V., and R. Sassen (2000), Thickness of the natural gas hydrate stability zone, Gulf of Mexico continental slope, *Mar. Pet. Geol.*, *17*, 981–991.
Milkov, A. V., and R. Sassen (2003), Two-dimensional modeling of gas hydrate decomposition in the northwestern Gulf of Mexico: Significance to global change assessment, *Global Planet. Change*, *36*, 31–46.
Miller, K. G., M. A. Kominz, J. V. Browning, J. D. Wright, G. S. Mountain, M. E. Katz, P. J. Sugarman, B. S. Cramer, N. Christie-Blick, and S. F. Pekar (2005), The phanerozoic record of global sea-level change, *Science*, *310*, 1293–1298.
Nagihara, S., J. G. Sclater, L. M. Beckley, E. W. Behrens, and L. A. Lawver (1992), High heat-flow anomalies over salt structures on the Texas continental slope, Gulf of Mexico, *Geophys. Res. Lett.*, *19*, 1687–1690.
Nimblett, J., and C. Ruppel (2003), Permeability evolution during the formation of gas hydrates in marine sediments, *J. Geophys. Res.*, *108*(B9), 2420, doi:10.1029/2001JB001650.
Nunn, J. A., and R. Sassen (1986), Framework of hydrocarbon generation and migration, Gulf of Mexico continental slope, *AAPG Bull.*, *70*, 1187–1187.
Piggott, N., and A. J. Pulham (1993), Sedimentation rate as the control on hydrocarbon sourcing, generation and migration in the deepwater Gulf of Mexico, Gulf Coast Section SEPM Foundation Fourteenth Annual Research Conference, pp. 179–191.
Pinero, E., M. Marquardt, C. Hensen, M. Haeckel, and K. Wallmann (2013), Estimation of the global inventory of methane hydrates in marine sediments using transfer functions, *Biogeosciences*, *10*, 959–975.
Pinero, E., C. Hensen, M. Haeckel, W. Rottke, T. Fuchs, and K. Wallmann (2016), 3-D numerical modelling of methane hydrate accumulations using PetroMod, *Mar. Pet. Geol.*, *71*, 288–295.
Prather, B. E. (2003), Controls on reservoir distribution, architecture and stratigraphic trapping in slope settings, *Mar. Pet. Geol.*, *20*, 529–545.
Rempel, A. W., and B. A. Buffett (1997), Formation and accumulation of gas hydrate in porous media, *J. Geophys. Res.*, *102*, 10,151–10,164.
Rice, D. D. (1980), Chemical and isotopic composition of natural gases in offshore Gulf of Mexico, *Abstr. Pap. Am. Chem. Soc.*, *179*, 6-GEOC.
Salvador, A. (1991), Geol. Soc. Amer., Geology of North America, vol. J, 568 pp., The Gulf of Mexico basin, Boulder, Colo.
Sassen, R. (1990), Lower tertiary and upper cretaceous source rocks in Louisiana and Mississippi—Implications to Gulf of Mexico crude oil, *AAPG Bull.*, *74*, 857–878.
Sassen, R., and I. R. Macdonald (1994), Evidence of structure H hydrate, Gulf of Mexico continental slope, *Org. Geochem.*, *22*, 1029–1032.
Sassen, R., S. T. Sweet, A. V. Milkov, D. A. DeFreitas, and M. C. Kennicutt (2001), Thermogenic vent gas and gas hydrate in the Gulf of Mexico slope: Is gas hydrate decomposition significant?, *Geology*, *29*, 107–110.
Sassen, R., A. V. Milkov, E. Ozgul, H. H. Roberts, J. L. Hunt, M. A. Beeunas, J. P. Chanton, D. A. DeFreitas, and S. T. Sweet (2003), Gas venting and subsurface charge in the Green Canyon area, Gulf of Mexico continental slope: Evidence of a deep bacterial methane source?, *Org. Geochem.*, *34*, 1455–1464.
Sawyer, D. S., R. T. Buffler, and J. R. H. Pilger (1991), The crust under the Gulf of Mexico Basin, in *The Gulf of Mexico Basin, Geol. of North Am.*, edited by A. Salvador, pp. 53–72, Geol. Soc. of Am.
Schroeder, W. W., A. W. Shultz, and O. H. Pilkey (1995), Late quaternary oyster shells and sea-level history, inner shelf, northeast Gulf of Mexico, *J. Coastal Res.*, *11*, 664–674.
Seol, Y., and T. J. Kneafsey (2011), Methane hydrate induced permeability modification for multiphase flow in unsaturated porous media, *J. Geophys. Res.*, *116*, B08102, doi:10.1029/2010JB008040.
Shedd, W., R. Boswell, M. Frye, P. Godfriaux, and K. Kramer (2012), Occurrence and nature of "bottom simulating reflectors" in the northern Gulf of Mexico, *Mar. Pet. Geol.*, *34*, 31–40.
Simms, A. R., N. Aryal, Y. Yokoyama, H. Matsuzaki, and R. Dewitt (2009), Insights on a proposed mid-Holocene highstand along the northwestern Gulf of Mexico from the evolution of small coastal ponds, *J. Sediment. Res.*, *79*, 757–772.
Stephens, B. P. (2001), Basement controls on hydrocarbon systems, depositional pathways, and exploration plays beyond the Sigsbee Escarpment in the central Gulf of Mexico, paper presented at Proceedings of the 21st Annual Gulf Coast Section of the Society of Economic Paleontologists and Mineralogists Foundation. Bob F. Perkins Research Conference, Soc. of Econ. Paleontol. and Mineral. Found., Houston, Tex.
Stephens, B. P. (2009), Basement controls on subsurface geologic patterns and coastal geomorphology across the northern Gulf of Mexico: Implications for subsidence studies and coastal restoration, *Gulf Coast Assoc. Geol. Soc. Trans.*, *59*, 729–751.
Torres, M. E., J. McManus, D. E. Hammond, M. A. de Angelis, K. U. Heeschen, S. L. Colbert, M. D. Tryon, K. M. Brown, and E. Suess (2002), Fluid and chemical fluxes in and out of sediments hosting methane hydrate deposits on Hydrate Ridge, OR, I: Hydrological provinces, *Earth Planet. Sci. Lett.*, *201*, 525–540.

Van Avendonk, H. J. A., G. L. Christeson, I. O. Norton, and D. R. Eddy (2015), Continental rifting and sediment infill in the northwestern Gulf of Mexico, *Geology*, *43*(7), 631–634.

Vion, A., and L. Menot (2009), Continental margins between 140m and 3500m depth. [Available at http://www.marineregions.org/ IFREMER.]

Wallmann, K., G. Aloisi, M. Haeckel, A. Obzhirov, G. Pavlova, and P. Tishchenko (2006), Kinetics of organic matter degradation, microbial methane generation, and gas hydrate formation in anoxic marine sediments, *Geochim. Cosmochim. Acta*, *70*, 3905–3927.

Wallmann, K., E. Pinero, E. Burwicz, M. Haeckel, C. Hensen, A. Dale, and L. Ruepke (2012), The global inventory of methane hydrate in marine sediments: A theoretical approach, *Energies*, *5*, 2449–2498.

Weimer, P., M. G. Rowan, B. C. McBride, and R. Kligfield (1998), Evaluating the petroleum systems of the northern deep Gulf of Mexico through integrated basin analysis: An overview, *AAPG Bull.*, *82*, 865–877.

Witrock, R. B., L. D. Nixon, P. J. Post, and K. M. Ross (2003), Biostratigraphic chart of the Gulf of Mexico offshore region, Jurassic to Quaternary, U.S. Dep. of the Inter., Bur. of Ocean Energy Manage., Regul. and Enforcement, New Orleans, La.

Wright, E. E., A. C. Hine, S. L. Goodbred, and S. D. Locker (2005), The effect of sea-level and climate change on the development of a mixed siliciclastic-carbonate, deltaic coastline: Suwannee River, Florida, USA, *J. Sediment. Res.*, *75*, 621–635.

Wygrala, B. P. (1989), Integrated study of an oil field in the southern Po Basin, Northern Italy, PhD thesis, Univ. of Cologne, Cologne, Germany.

Zhang, Z. J., D. H. Han, and Q. L. Yao (2011), Quantitative interpretation for gas hydrate accumulation in the eastern Green Canyon Area, Gulf of Mexico using seismic inversion and rock physics transform, *Geophysics*, *76*, B139–B150.

Zhang, Z. J., D. R. McConnell, and D. H. Han (2012), Rock physics-based seismic trace analysis of unconsolidated sediments containing gas hydrate and free gas in Green Canyon 955, Northern Gulf of Mexico, *Mar. Pet. Geol.*, *34*, 119–133.